Spectroscopic Studies of Silver Bromo-Iodide Crystals: Photoluminescence Temperature Dependence of Iodide Quantum Clusters as Tabular Grain Defects

S. H. Ehrlich*

Manufacturing Research and Engineering Organization, Eastman Kodak Company, Rochester, New York, 14650-1736

Photoluminescence (10 to 90 K) processes resulting from recombination centers emitting in the region of 550 nm in <III> AgBr (88%)–I (12%) tabular grains are studied. Stacking faults, dislocation defects, or double-twin planes are present in these microcrystallites. The greater the number and kind of iodide defects, the higher the low-temperature fluorescence quantum efficiency. The second-derivative photoluminescence presents additional information of competing emitting Ag_3° R-type centers emitting in the region of 562 to 571 nm. The photophysical processes leading to photoluminescent centers relate to emulsion-making conditions involving iodide clustering, not AgI phases. It is the differences of ΔE of the rate-determining step that influence the quantum efficiency of fluorescence in the various low-temperature regions: 0.0009 and 0.0007 eV below 30 K, and 0.065 and 0.055 eV in the 50 to 70 K region for minimal defect and S-defect tabular grains. The 0.065 and 0.055 eV are shallow electron traps beneath the conduction band. The βAgI hexagonal fine grains of 36 Å diameter were assigned to the quantum particle (confinement) fluorescence at 424 nm and a βAgI large-grain 448-nm Stokes-shifted emission; γAgBr emission for microcrystals is 455 nm. The quantum model, using effective masses, describes Wannier excitons of I_m^{n-} in AgBr. The structure of clusters seems to consist of bent, 3-at. iodide structures $(AgI_3)_n$. Also, clusters consist of 3-at. linear configurations, formed during the emulsion-making process, and emitting radiation in the region of 540 and 590 nm with cluster diameters of 12 to 14 Å, respectively. These clusters $(AgI_3)_n$ or $(^+AgI^- - I_2)_n$ interact closely with the AgBr point defect lattice. Recombination emission from these clusters is studied. Microcrystals containing double-twin planes have an additional excitation band coincident with the emission band at 461.5 nm (2.6860 eV), the exciton localization at the twin plane. The higher energy excitation is shown at 461.0 nm (2.6889 eV), the assigned indirect exciton band gap. Splitting of 2.9 MeV or hole-limiting binding energy to the iodide anion located at the twin plane provides an estimate of the hole lifetime of 1.41×10^{-10} s at 10 K. The hole and electron are capable of traversing the double-twin plane separation of 93.3 and 100 Å.

Journal of Imaging Science and Technology 41: 13–29 (1997)

Introduction

The silver bromo-iodide tabular grains are used as an important photographic light-sensing element. Numerous investigations of iodide-related luminescence AgBr have been published.[1–17] In these studies, a temperature dependence of fluorescence emission from iodide centers is performed on AgBr,I tabular grain emulsions to detect the nonhomogeneous iodide incorporation related to defect structures or emulsion-making procedures and possibly to the sizes of the iodide clusters.[1a,b,d] Low-temperature fluorescence spectroscopy was used to detect bulk and interfacial iodide species, silver aggregates, domains, or quantum-size clusters formed during the photographic emulsion-making process.[1a,b,d]

In mixed-halide emulsions containing iodide, the importance of iodide is its influence on spectral sensitization, light absorption, chemical sensitization, pressure sensitivity, and developability. Low-temperature steady-state spectroscopy was used to determine the recombination process for the electron in the conduction band of the AgBr,I microcrystallite and the emitting-iodide centers within the band gap.[14] A rapid-iodide addition, (RIA), subsurface treated with 0.3 mol KI/Ag mol/5 s for 3%, to the emulsion resulted in a fluorescence emission at approximately 590 nm compared with the run-iodide (R) emulsion emission in the region of 540 nm.[1a,b] In the past, low temperature (6 K) photoexcitation and photoluminescence spectra have been obtained for a number of single crystals, sheet crystals, run, run-plus-rapid-iodide additions, and core-shell AgBr,I emulsions.[18] Calibration curves were derived from single crystal and run-iodide emulsions. The calibrations related the emission-band maximum to iodide concentration. The iodide concentration in emulsions containing heterogeneous bromo-iodide regions is determined from the calibrations.[18] The Stokes' shifts were constant for a wide concentration range of run-iodides, but varied considerably when heterogeneous bromo-iodide emulsions were studied. The difference was interpreted as arising from interfacial species.[18] Koitabashi and Harada[19] showed similar fluorescence spectral energy shifts as a function of iodide concentration with excitation at 337 nm and 4.2 K, but without the long-wavelength (590 nm) emissions.

Belous et al.[1d] describe the microcrystals of hexagonal βAgI and cubic γAgI showing luminescence spectra with maxima at 421, 455 to 460, and 440 to 445 nm, respectively. These authors also related the 77 K emission bands to the emulsion AgBr,I microcrystal cubic and octahedral formation process after addition of iodide with subsequent addition of KBr. The βAgI phase was diminished spectrally in amplitude as the iodide phase recrystallized and formed paired iodine centers with enhanced emission noted at 550 nm after making of the emulsion continued with the addition of KBr for 40 min. It appears that the precipitated phase of AgBr is an aggregate of both β on the hexagonal faces {111} and γAgI on the cubic faces {100} and that under selected conditions for the formation of emulsions, γAgI

Original manuscript received February 28, 1996. Revised September 20, 1996.

* IS&T Fellow

dissolves faster. Another experiment[1d] related AgBr,I emulsions to process mechanisms of AgI and showed that when there is an excess of silver ions (pAg = 2 and 3) the spectra have a band (λ_{max} = 440 nm) that is characteristic for γAgI. If, on the other hand, these emulsions were made with excess iodide ions (pI = 2, 3, and 4), then the luminescence spectra reveal one of the peaks (λ_{max} = 445 to 460 nm) to be that of the βAgI microcrystalline phase. Also present under βAgI formation conditions are the 550- and 610-nm prominent bands when KI solution (pI = 3) is in contact with the emulsion for 5 min.

In the present study the γ and βAgI phases have not been observed. Instead, the commonly prominent 550-nm region is eminent, due to the loss in recrystallization of the βAgI phase as bromide ions are added, and is described in terms of iodide clusters, not phase separation. Iodide clusters have been studied with respect to size and shape within the solid phase.[4b] In a later section, this author will show βAgI and γAgI crystal phase photoluminescence emission bands that are attributed to 448 (Ref. 16a) and 455 nm, respectively, in contrast to the above assignment.[1d]

Therefore, a study of low-temperature photoluminescence can provide electronic properties of heterogeneous emulsion grains, as well as insight into the determination of the iodide concentration associated with the different methods of introduction into the grain.[1a,b,d] A luminescence band at 495 nm results from the presence of relatively pure bromide regions in heterogeneous silver bromo-iodide emulsions. The trace amounts of iodide in this region give rise to an iodide-bound exciton emission and, at 520 nm, to an exciton bound to an iodide pair.[8,12] A low-iodide-concentration band results from iodide diffusion into the bromide phase during precipitation. The intensity of the low-concentration-iodide band at 530 to 540 nm decreases as the iodide run time increases, which results in the predominance of a high-concentration-iodide band at 590 nm.[18] The assignment of a high-iodide concentration is in apparent conflict with Moser and Lyu,[8] who observed the 590-nm luminescence band on AgBr sheet crystals containing 5×10^{-6}, 5×10^{-5}, and 5×10^{-4} mol fraction iodide. However, if small concentrations of iodide were localized at defect sites or at grain boundaries as clusters, the appearance of the 590-nm band would support Ehrlich's iodide-cluster-formation hypothesis.[1a,b]

Burberry[2] also demonstrated the same band on sheet crystals of less than 0.0001 I^- mol fraction when analyzed by neutron activation.

Results of core-shell emulsion with a high-iodide core and low-iodide or pure bromide shells have been interpreted as the iodide interior gradient spreading toward the outer layers and thus forming a diffuse interface.[20] This structure is apparently supported by ion-scattering spectroscopy results that show the presence of iodide at the grain surface of core-shell emulsions when the shell is not sufficiently thick.[20] Several mechanisms of iodide enrichment at the surface have been proposed, but the exact mechanism is still to be determined.[1,20] Note that the mean solid-state iodide diffusion three-dimensional distance is $(6Dt)^{1/2}$ or 6.4×10^{-8} cm (6.4 Å) for $t = 8.6 \times 10^{+4}$ s (1 d) at 97.2°C, where D is 8×10^{-21} cm^2/s. Therefore a room-temperature thermalized migration could be considered negligible.[21] A previous study by Ehrlich[1b] of the low-temperature photoluminescence peak intensity when excited with energy sufficient for the band-to-band transitions in AgBr,I with varying intensities, showed linearity at 498 nm for the bound-iodide exciton. However, in the region of 586 to 604 nm, without interfering iodide luminescence, the emission with trace iodides shows quadratic intensity dependence.[1b] This region of emission has been assigned to silver-cluster-to-valence-band recombination from linear 3-at. unstable R centers and 4-at. P centers of bent clusters of 2 (Ag_2°) not iodide.[1a] These clusters interact closely with specific orientation to the AgBr lattice planes and defects therein and have diameters of 9.18 to 10.6 Å with photoluminescence in the region of 563 to 760 nm.[1a] The bent silver cluster double dimers coincide very closely to angles of 45° and 54.7° and to the {100} to {110} and {100} to {111} planes with photoluminescence assigned at 700 to 760 and 563 to 620 μm, respectively.[1a] The intrinsic band-gap absorption relates the P and R silver cluster HOMOs to the valence band. The photon absorption places the silver cluster LUMO of the R center slightly above and the P center below the conduction band, respectively.[22] However, hole injection to the HOMO of the R center provides a possible recombination pathway and would position several emitting LUMO energy levels 0.31 eV closer to the conduction band.[22] Several conclusions have been drawn by Ehrlich.[1a,b]

1. The large Stokes' shifts that exist in homogeneous run-iodide dispersions of AgBr are enhanced with an increase in temperature, indicative of different cluster sizes. Heterogeneous rapid-iodide addition shows greater Stokes' shifts, as observed in the 580 to 600-nm region, and provides evidence that more closely associated clusters of iodide are present.[1a,b] Under ripening conditions, a long-wavelength photoluminescence band may be reduced and shifted to shorter wavelengths of the 530- to 540-nm region. It is the reorganization of these larger quantum-sized clusters into smaller groups, which are less associated, that provides the complex spectra. The emission spectra are not that of AgI, but instead are of discrete iodide clusters within the defect AgBr lattice.
2. The photoluminescence of the higher temperature spectral profiles of tabular and octahedral grains of run iodide shows clusters of iodide similar to those of the low-temperature rapid-iodide addition.
3. The existence of quantum-size clusters of iodide is reinforced by the nonlinear concentration dependence in the run-iodide studies as well as by the rapid-iodide-addition comparisons.
4. The basic photophysical processes leading to photoluminescence relate to emulsion-making iodide conditions and are similar for cubic, octahedral, and tabular-grain morphologies.
5. The higher temperature iodide emission quenching of the rapid-iodide addition results in the observation of a 580 to 590-nm-region band assigned to silver-cluster formation; e.g., 1.25 mol% run iodide and 1.75 mol% rapid-iodide addition of 0.58-nm octahedral grains.[1b]
6. A graph of the peak luminescence positions of AgBr,I versus lattice constant provides data from the photoluminescence energy spectra and the immediate correlation with the expansion of the lattice caused by incorporated iodide concentrations.
7. The quantum model of a particle-in-a-box provides ideal structural information, bent and linear configurations of iodide clusters, that agree with the experimental data. A deviation is observed for the bound exciton diameter. The clusters of iodide have been estimated to be 8 to 13 Å in diameter.

When iodide concentration (3 to 18 mol%) is incorporated into AgBr lattice, structural defects can be observed by transmission electron microscopy (TEM), with the detection of existing stacking fault/dislocation defects within

the AgBr,I crystallites (This is the case with homogeneous addition of iodide in the shell of the AgBr–AgBr,I core-shell-type tabular microcrystal.) Tabular silver bromide grains with iodide uniformly mixed in the shell were investigated with conventional transmission electron microscopy. The shell region contained a large number of stacking faults parallel with the $\{11\bar{1}\}$ edges and, in some cases, edge dislocations with a Burgers vector of 1/2-MG $[1\bar{1}0]$ type. An atomic model for the formation of the stacking[23] faults during growth is presented relative to the interfacial planes. A model for the disappearance of stacking faults, which involves the movement of partial dislocations in the stacking fault plane, is presented in a temperature study of the AgBr–AgBr,I (10% I) tabular core-shell microcrystals.[24] The stacking faults that are present in the shell of the microcrystal disappear when the microcrystals are heated to 200°C and higher. The stackings are removed most easily from parts with only one reentrant angle at the twin planes, i.e., in hexagonal microcrystals or at long segments of triangular microcrystals.[24] In the past, extensive studies on tabular microcrystals have been published on crystallography[25,26] and morphology.[27a,b] Also stacking fault excitons were studied extensively in BiI_3 and GaSe by the appearance of characteristic sharp lines in the optical absorption and emission spectra just energetically below the indirect exciton edge.[28] The excitonic properties of AgBr, an indirect-band-gap semiconductor 2.6845 eV (461.76 nm) with weak absorption spectrum, have been studied by emission spectroscopy for free and weakly bound excitons observed energetically below the indirect exciton band gap.[29a] Excitation spectroscopy has been used to examine the absorption of AgBr in the region of the indirect band gap.[29b] The indirect exciton absorption involving the double-twin planes in this study should be observed in the excitation spectrum caused by the symmetry change of the twin plane formation and by monitoring the recombination iodide cluster emission (554 nm $\approx$ 2.24 eV).[1b] The high-resolution excitation spectrum would detect defects in, or near, the twin planes under growth conditions if the iodide anions were incorporated. Two structural defects are associated with run-iodide AgBr,I. The first, Sample 2, has a striation-like contrast (three-fold symmetry) parallel to the grain edges and with adjacent contrast lines separated by ~0.01 nm (S-defect), and the second, Sample 1, devoid of striations, has a two-dimensional gridlike contrast, onefold, or P1 symmetry, dispersed across the entire grain. These defects are separated from each other by a spacing of ~6 to 7 nm.

The photoluminescence temperature study also involves the following: (1) a second-derivative comparison between Sample 2 and 1; (2) a proposed electron-trapping model; (3) photoluminescence quantum efficiency and an activation energy determination for shallow electron-trapping levels beneath the conduction band; (4) a suggested correlation between nanocluster shape, size, and emission energy; and (5) the proposed relationship between the second-derivative photoemission, excitation spectra, and the double-twin planes within the microcrystals. In this initial photoluminescence temperature-dependent study, a comparison is made between a double-jet $AgBr_{0.88}I_{0.12}$ (after nucleation and partial growth) containing an abundance of striation-like contrast defects, Sample 2, and a dual zone, spatial separation of nucleation and growth make $AgBr_{0.88}I_{0.12}$. These latter microcrystals contain almost no S-defect, Sample 1.

Experimental

Apparatus. The steady-state luminescence of nanoclusters was measured on the SLM-4800C spectrofluorometer. The transient absorption studies of cluster surface silver gold sulfides have also been reported previously.[5] The concentration of iodide per grain volume per coverage determines the fluorescence intensity of the signal. The sample, a film, was positioned within a cryostat, outside the sample chamber of the instrument, but optically excited via quartz fiber optics. Emission signals reentered the spectrofluorometer by a similar quartz optical fiber pathway. Condensing optics focused the emission onto an aberration-corrected holographic grating monochromator with a linear dispersion of 2 nm/mm. A broad spectral range of 200 to 850 nm and extremely low stray light made this monochromator desirable for these experiments. Signals were collected by the SLM noncooled R928 and EMI 9813QA photomultipliers in the emission monochromator and reference modules, respectively. The R928 photomultiplier is sensitive to 850 nm. Data from the SLM mainframe were transferred to an HP9815/IBM-PS2 computer with an HP7225A/HP Color Pro plotter for numerical correction, storage, and manipulation and for amplification of spectra, kinetics, and differential spectroscopy.

The following modifications were made on a CTI-Cryogenics closed-cycle refrigerator and sample-chamber configuration (Fig. 1):

1. Flanges attached to the cryostat were machined to incorporate quartz optics for focusing the exciting radiation and the emission of the emulsion samples. The flanged fiber optics were excited by the spectrofluorometer and entered the cryostat flange system. Thus the prefocused cryostat optics allowed both the alignment of the exciting radiation on the sample and the optical alignment of the emission signals through the quartz-fiber bundle to the spectrofluorometer.
2. The brass sample holder frame was divided into five sections, each section optically isolated, which held the film against the thermal reservoir. A thermal diode detector was incorporated into the holder and the temperature range controlled and monitored by a

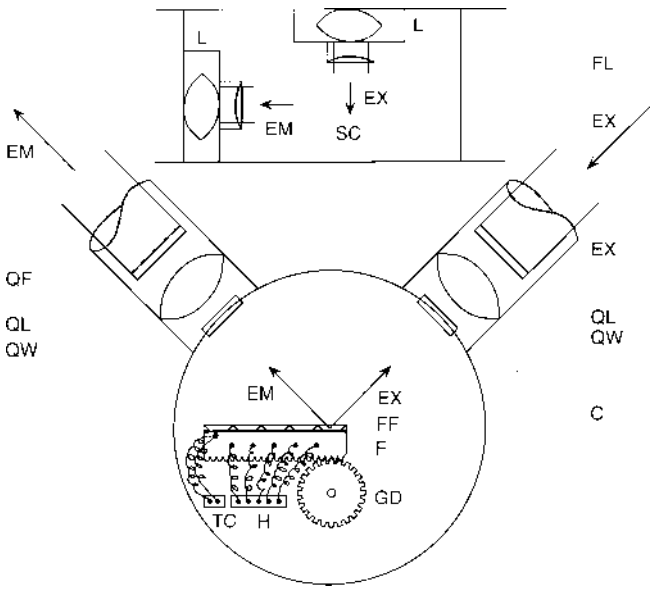

Figure 1. Low-temperature cryostat designed to obtain optical emission spectra of silver iodobromide emulsions: FL, spectrofluorometer; L, lens assembly; EX, excitation optics; EM, emission optics; SC, sample chamber; QF, quartz fiber bundle; QL, quartz lens; QW, quartz window; C, cryostat; FF, film frame holder; F, cold block; H, heater; TC, thermal diode detector; GD, gear drive.

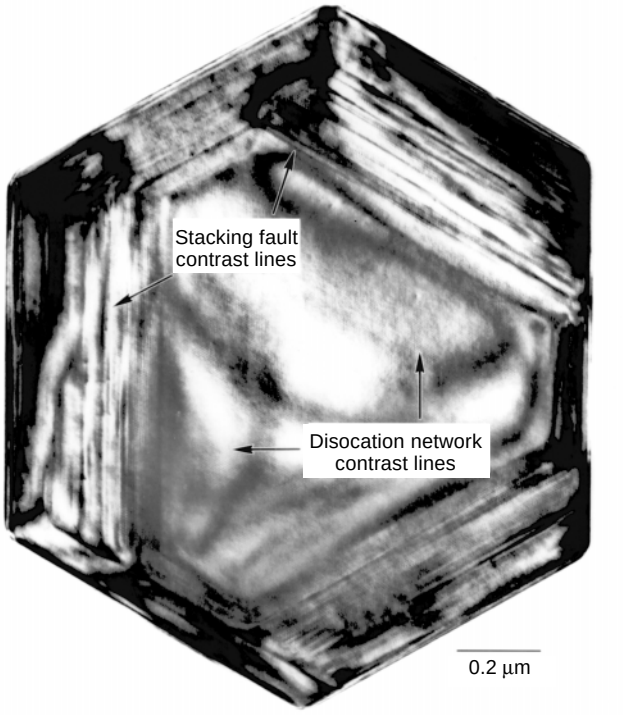

$AgBr_{0.88}I_{0.12}$ T-grain

Figure 2. Plan-view $(\bar{2}20)$ two-beam TEM image of a tabular grain made using standard double-jet precipitation, Sample 2, $AgBr_{0.88}I_{0.12}$, large amount of S-defect; diffraction contrast from the internal stacking faults and dislocation networks.

P. B. Cryophysics, Inc., Model 4025 thermometer controller. The temperature ranges monitored were 9.00 to 200.00 K ± 0.10 K.

3. The optical alignment of the sample position was performed electronically in response to the exciting radiation. The positioning of the film sample utilized a rack-and-pinion movement; thus, five vernier positions or five temperatures may be used to probe the total spectral fluorescence without changing the sample, the realigning, or without breaking the vacuum conditions.
4. The CTI-Cryogenics cryostat Cryo-Torr cold head was mounted outside the spectrofluorometer to prevent vibration misalignment.

Films were coated with gelatin microcrystallite dispersions of nonsensitized silver bromo-iodide. The emulsions were prepared with controlled variations in iodide incorporation. The excitation was at 400 ± 1.0 nm with an emission spectral resolution of 0.50-nm bandwidth. The photoexcitation spectra were compensated by a reference photomultiplier tube, the signal of which was stored and referenced with the emission spectra.

Emulsion Preparation. Emulsions for Samples 1 and 2 were made with identical dual-zone nucleations (separate nucleation and growth positions) with pure bromide. For Sample 1, after nucleation and stabilization of the pure bromide tabular nuclei, dual-zone growth with 1.5 mol% iodide was carried out for 10% of the total growth, followed by dual-zone growth with 12 mol% iodide for remainder of the growth. Sample 2, however, was made with 1.5 and 12 mol% iodide, double-jet, at 10% and 25% growth, respectively. The reactant concentrations, addition rates, and iodide distribution of Sample 2 (striations—S), Fig. 2, were the same as those of Sample 1 (devoid of striations—NS), Fig. 3, but the silver and halide reactants were introduced by the conventional double-jet addition process. Also, in the latter case, the gelatin solution that was used in the dual-zone process was introduced through surface addition away from the reaction zone. Plan-view observation was carried out on tabular grains of the above emulsions after extraction from their gelatin matrix by centrifugation. Observations were carried out at 200 kV accelerating voltage with the sample cooled by LN_2 to –180°C. The elemental compositions of Sample 2 (S) and Sample 1 (NS) were probed by x-ray energy dispersive spectroscopy. The coverage composition of the films were 200 mg/gel/ft^2 and 100 mg Ag/ft^2.

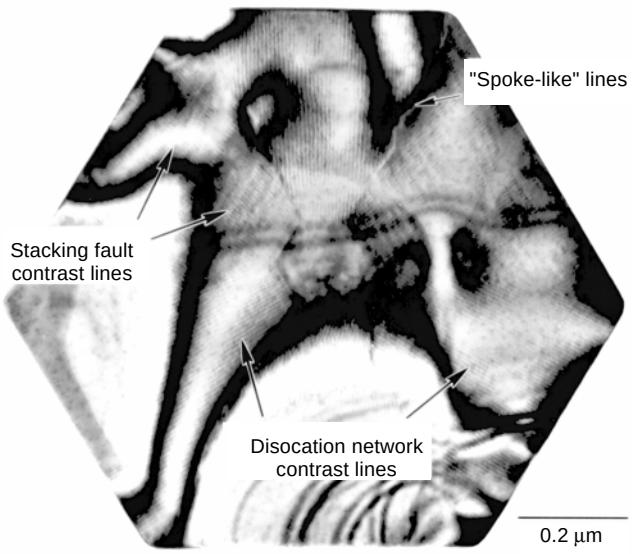

$AgBr_{0.88}I_{0.12}$ T-grain

Figure 3. Plan-view $(\bar{2}20)$ two-beam TEM image of a tabular grain, a dual-zone precipitation, Sample 1, $AgBr_{0.88}I_{0.12}$, small amount of S-defect.

The control microcrystallites of βAgI were made from the double-jet KI and $AgNO_3$ precipitation; nucleated at 50°C for 0.5% of the make at 1.12 g / ℓ KI, excess halide, (–200 mV) and grown for the remaining part of the precipitation at 75°C. The final crystals were wurtzite 0.67-μm hexagonal bipyramids. The γAgI sphalerite cubic micro-crystals of 0.15 μm were prepared in a similar way with excess silver ion (+500 mV).

The film samples were held 20 min at the equilibrium temperature before spectroscopic analysis proceeded; new sample positions were radiated for each temperature selected.

Results and Discussion

Photoluminescence and Derivative Spectroscopy.* Figures 4 through 8, dashed line, show the 10.0, 30.0, 50.0, 70.0, and 90.0 ± 0.1 K fluorescence spectra, excited at 400 nm, with an emission scan of 420 to 780 nm of Sample 2. The defect structure identified as striation-like features in plan-view TEM (Fig. 2) were made using the double-jet precipitation condition. The spectra are characterized as having an apparent major single peak at 554.0 (10 K), 559.0 (30 K), 560.0 (50.0 K), 565.0 (70 K), and 565.0 nm (90 K),

* The Savitzky-Golay algorithim software used within the SLM Spectrofluorimeter is based on work by A. Savitzky and M. J. E. Golay, *Anal. Chem*., **36**: 1627 (1964).

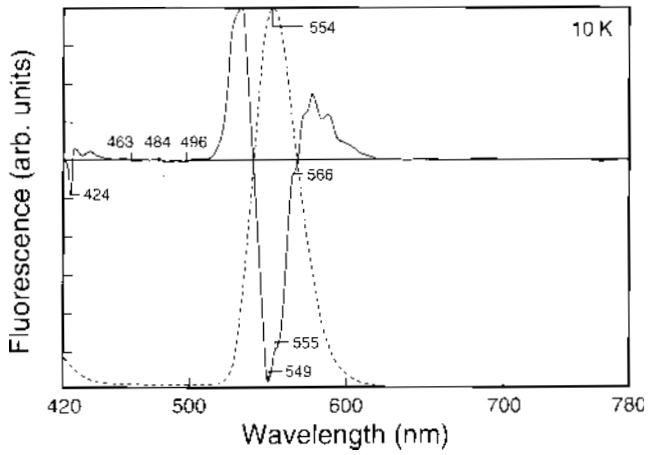

Figure 4. The low-temperature 10.0 ± 0.1 K photoluminescence, S-defects, tabular-grain $AgBr_{0.88}I_{0.12}$, AgBr core surrounded by AgBr,I shell (optically uncorrected, dashed line). The second-derivative photoluminescence S-defect spectrum (solid line).

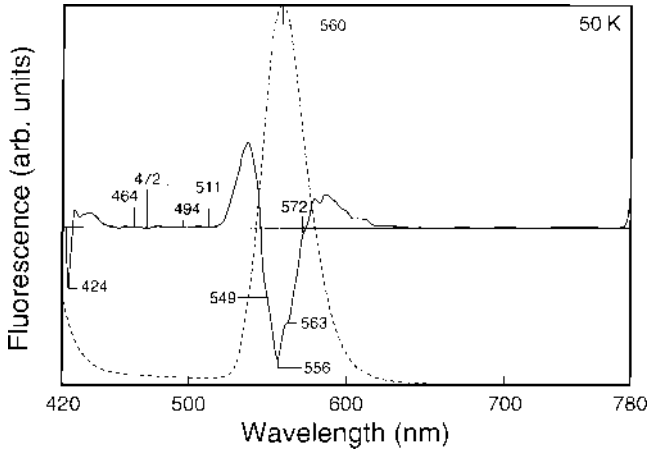

Figure 6. The low-temperature 50.0 ± 0.1 K photoluminescence, S-defects, tabular-grain $AgBr_{0.88}I_{0.12}$, AgBr core surrounded by AgBr,I shell (optically uncorrected, dashed line). The second-derivative photoluminescence S-defect spectrum (solid line).

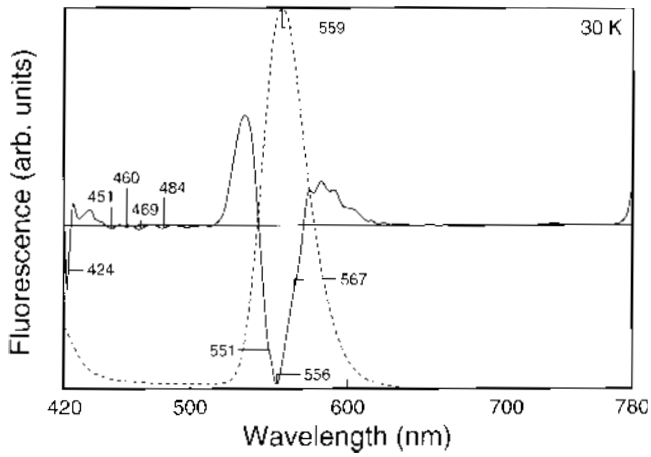

Figure 5. The low-temperature 30.0 ± 0.1 K photoluminescence, S-defects, tabular-grain $AgBr_{0.88}I_{0.12}$, AgBr core surrounded by AgBr,I shell (optically uncorrected, dashed line). The second-derivative photoluminescence S-defect spectrum (solid line).

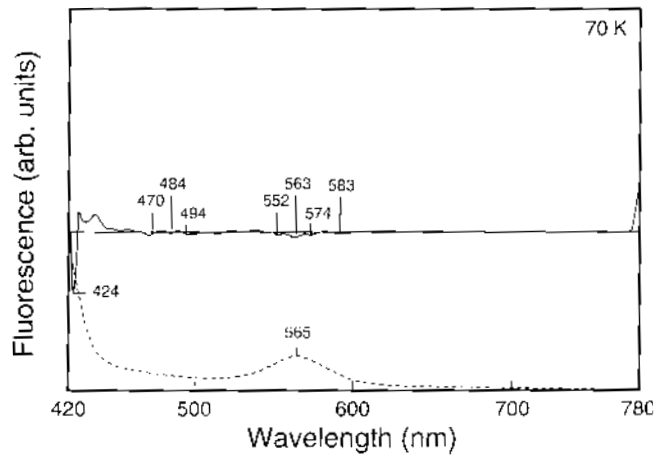

Figure 7. The low-temperature 70.0 ± 0.1 K photoluminescence, S-defects, tabular-grain $AgBr_{0.88}I_{0.12}$, AgBr core surrounded by AgBr,I shell (optically uncorrected, dashed line). The second-derivative photoluminescence S-defect spectrum (solid line).

respectively. These distinguishing wavelength features imply a run (R) homogeneous iodide (substitution for bromide) distribution in the shell of the crystallites a core-shell configuration.[1a,b] The second-derivative, Figs. 4 through 8, solid line, emission clearly differentiates at least three major spectroscopic structures because of iodide incorporation within the microcrystallites: 549, 555, and 566 nm (10 K) 551, 556, and 567 nm (30 K); 549, 556, and 563 nm (50 K). A subtle shoulder at 570 to 572 nm is also observed at 50 K. The low-signal 70 K s derivative contains three small signals: 552, 563, and 574 nm. A smaller signal is also evident at 583 nm. The 90 K minimal emissions observed show a 556, 565, and 572-nm signal with a subtle shoulder to a longer wavelength; i.e., 585 nm. The subtle second-derivative signals that are in the range of 460 to 470 nm will be investigated later in this paper. The photoluminescence of subtle peaks between 570 to 585 nm are attributed to small Ag°_{n} clusters.[1a,b] Figure 9 shows the uncorrected photoluminescence spectra of the 10 to 90 K striation microcrystallites. Figure 10 shows the excitation spectrum, (Sample 2) 350 to 450 nm, inset 9.5 K, monitored at 554-nm emission.

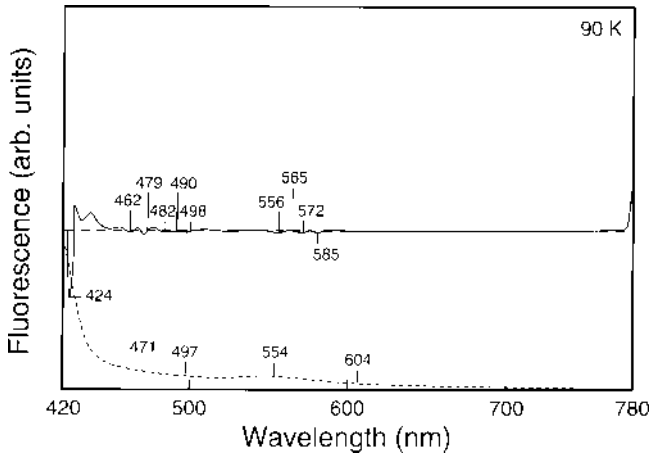

Figure 8. The low-temperature 90.0 ± 0.1 K photoluminescence, S-defects, tabular-grain $AgBr_{0.88}I_{0.12}$, AgBr core surrounded by AgBr,I shell (optically uncorrected, dashed line). The second-derivative photoluminescence S-defect spectrum (solid line).

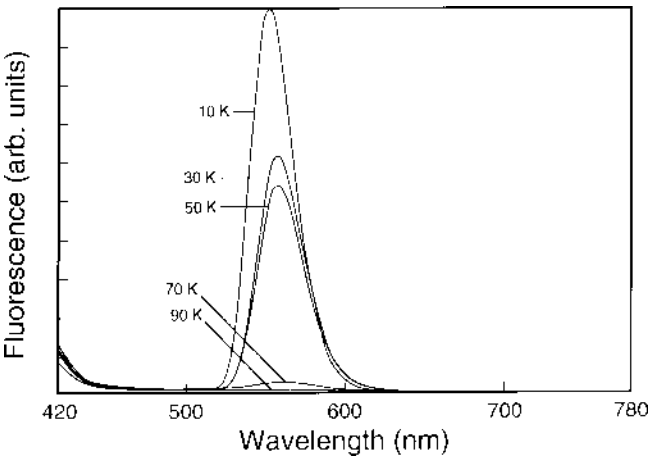

Figure 9. The optically uncorrected, low-temperature 10 to 90 K photoluminescence, S-defect spectra of $AgBr_{0.88}I_{0.12}$, tabular-grain 420 to 780 nm with excitation of 400 nm.

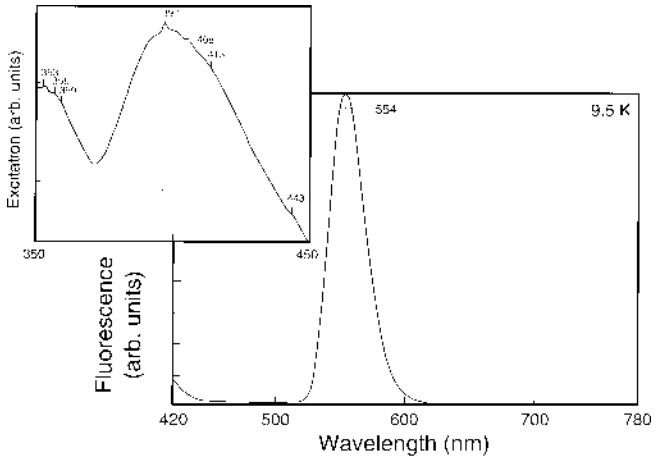

Figure 10. The excitation spectrum, inset, (Sample 2) at 350 to 450 nm, 9.5 K, monitored at 554-nm emission. The excitation spectra were similar for 549- and 566-nm emissions.

βAgI and γAgI Emission. Figure 11(a), the absorption spectrum of βAgI, 0.67-μm hexagonal bipyramid, (wurtzite W) of 350 to 450 nm suggests small βAgI crystallites, 36 Å diam (discussed relative to Fig. 29 shown later in the article) existing off the surface of the grains when the photoluminescence is monitored at 424 nm (excitation 390 nm) and is observed in all second-derivative low-temperature traces, e.g., Fig. 11(b). The 10 K photoluminescence of βAgI shows the 424 nm and exciton large-grain 448-nm Stokes-shifted emission (dashed line) and the second-derivative of the pure sample crystallites, Fig. 11(d) (solid line). This emission has been observed by T. M. Mashlyatina and colleagues.[16a,b] The x-ray diffraction is also shown for the pure βAgI [Fig. 11(c)]. Figure 11(e) describes the 10 K photoluminescence of γAgI microcrystals in gelatin exhibiting a 455-nm maximum with a second-derivative band at 454 nm; a minor emission peak observed near 525 nm is assigned to Ag_n° clusters. Figure 11(f) shows the x-ray diffraction pattern of a mixture of βAgI and γAgI (sphalerite) cubic crystals in gelatin prepared with a silver ion excess in gelatin at +500 mV sized at 0.15 μm. The major species is γAgI.

Figures 12 through 16, dashed line, show the 10.0, 30.0, 50.0, 70.0, and 90.0 ± 0.1 K fluorescence spectra excited at 400 nm of Sample 1. The defect structure contained almost minimal S-defect (NS)-like features in plan-view (Fig. 3) TEM, made after the nucleation and stabilization of the pure bromide tabular nuclei, dual-zone growth, with 1.5 mol% iodide carried out for 10% of the total growth, followed by dual-zone growth with 12 mol% iodide for the remainder of the growth. We should state again that the reactant concentration addition rates, and iodide distribution of Sample 2 were the same as those of Sample 1, but the silver and halide reactants were introduced by the conventional double-jet addition process for Sample 2. Also, in the Sample 1 case, the gelatin solution used in the dual-zone process was introduced through the surface addition, away from the reaction zone.

The spectra are again characterized as having an apparent major, single peak at 550.0 (10 K), 553.0 (30 K), 556.0 (50, 70 K), and approximately 553.0 nm (90 K), respectively. The position of this band again erroneously implies a run (R) iodide homogeneous substituted distribution in the shell of the crystallite core-shell configuration. The second-derivative, Figs. 12 through 16, solid line, photoluminescence, again, clearly differentiates at least two major spectroscopic structures relating to iodide incorporation within the microcrystallites: 544, 550, and 561 nm (10 K), 546, 551, and 565 nm (30 K); and 549, 555, and 563 nm (50 K). A detectable shoulder at 571 nm is seen at 50 K, indicative of small Ag_n° clusters.[1a] A small luminescence signal is detected in the 540 to 600 nm region at 70 K. Likewise, the photoluminescence for the 90 K second-derivative is not observable in Fig. 16 under the same conditions for Sample 2 detection. The βAgI microcrystallites, 36 Å diam, are present in the gelatin for all samples, as shown by the 424-nm second-derivative photoluminescence band.

Figure 17 is the uncorrected, 10 to 90 K, photoluminescence spectra of the minimal striation (NS) microcrystallites.

Figure 18 is the excitation spectra, at 9.50 ± 0.1 K, of the 550, 555, and 566 nm photoluminescence of the second-derivative. Shown are three similar spectra, 350 to 450 nm, with specific broad maxima at approximately 355, 398, and a shoulder at 412 and 443 nm, respectively, for NS microcrystallites. The excitation spectra are similar for each of the luminescence wavelengths given above. Attempts to find an optical absorption or excitation band characteristic of each of the photoluminescent centers were unsuccessful. Simultaneous thermoluminescence (TML) and thermally stimulated current (TSC) experiments suggest that free carriers participate in the luminescence; they do not preclude the possibility that excitons[29–31] rather than free carriers are initially formed by the exciting radiation. In the free-carrier case, the intermediate state, the conduction band would negate the direct relation of the excitation and emitting centers.[1a,b] The excitation spectra should be probed more carefully, as shown in a later section, with a view toward exciton migration. The multiple emitting centers shown in the second-derivative photoluminescence spectra are indicative of various iodide cluster sizes and orientations.[1a,b]

The quantum clusters of iodide are within the tabular crystallites noted at 549, 556, and 563 nm; the Ag_3° clusters are evident at 571 nm.[1a,b]

Temperature Dependence. Figure 19 shows the steady-state peak photoluminescence (signal voltage) in vacuum of $AgBr_{0.88}I_{0.12}$ S-defect, Sample 2 (551 to 556 nm) and minimal S-defect, Sample 1 (554 to 560 nm), 10 to 90 K, respectively. The striking feature of both Samples 2 and 1 is the two recombination plateau regions, 30 to 50 K and 70 to 90 K with emission intensity of Sample 2 » Sample 1. These data are optically corrected for sample position as the unexposed sample is traversed into the optical beam.

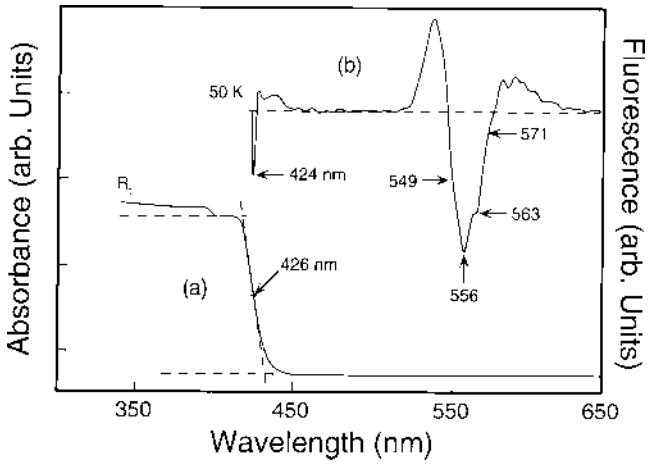

(a, b)

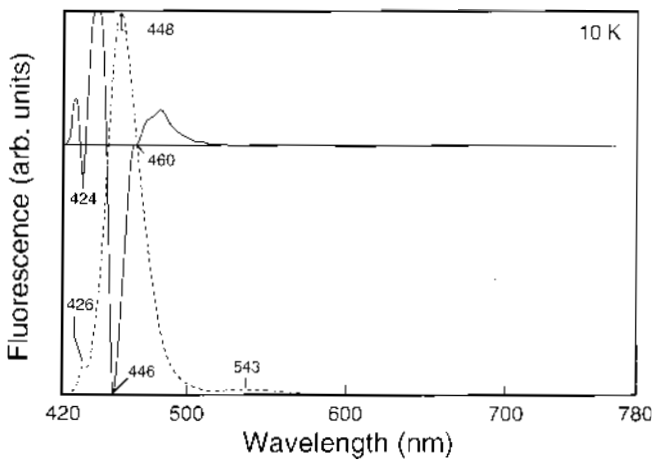

(d)

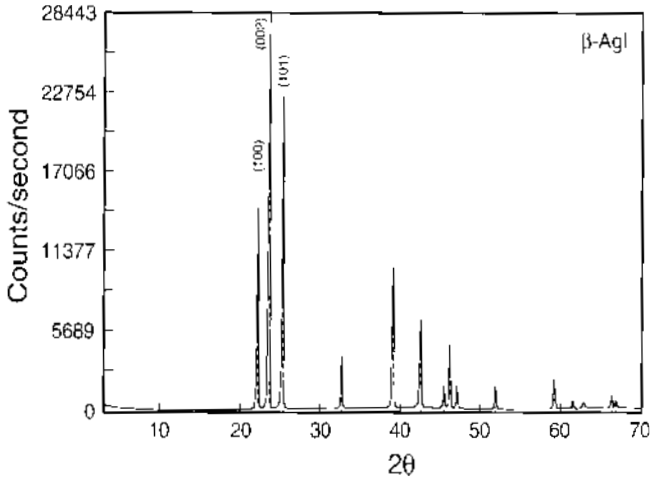

(c)

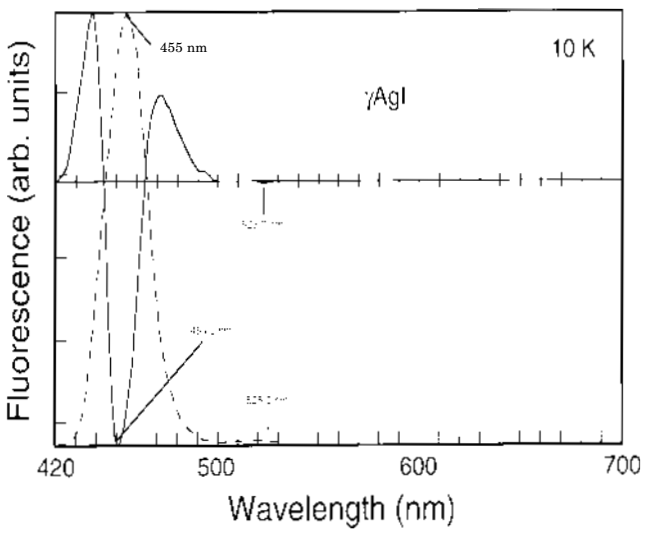

(e)

Figure 11. (a) The 25°C absorption broad spectrum 350 to 410 nm, β′AgI, 0.67-μm hexagonal bipyramidal (wurtzite W) crystallites in gelatin 426-nm band edge; (b) The second-derivative 50 K photoluminescence of S-defect tabular-grains, 424- and 556-nm emission: excitation 390 nm; (c) X-ray diffraction pattern of pure βAgI (wurtzite) hexagonal bipyramidal crystals in gelatin; (d) 10 K photoluminescence, βAgI in gelatin, dashed line, 426- and 448-nm maxima; second-derivative, solid line, 446-nm maxima (Note: 424- and 446-nm band), excitation at 390 nm; (e) 10 K photoluminescence, γAgI in gelatin, dashed line with maxima at 455- and minor 525-nm band; second-derivative, solid line 454-nm maxima with a minor 523-nm band, excitation at 390 nm (preparation with excess silver ion in gelatin at +500 meV); (f) X-ray diffraction pattern of pure γAgI (sphalerite) cubic crystals in gelatin.

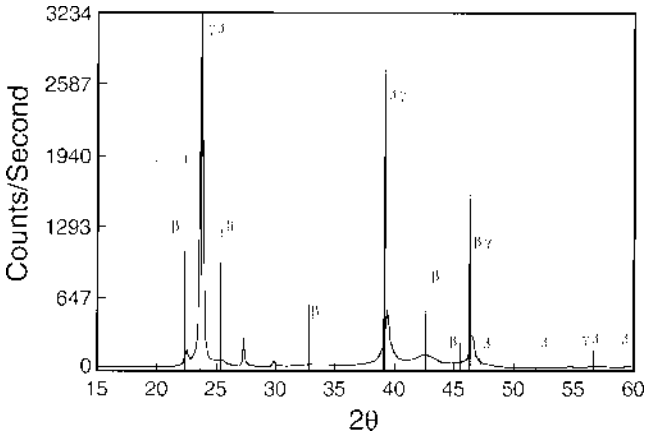

(f)

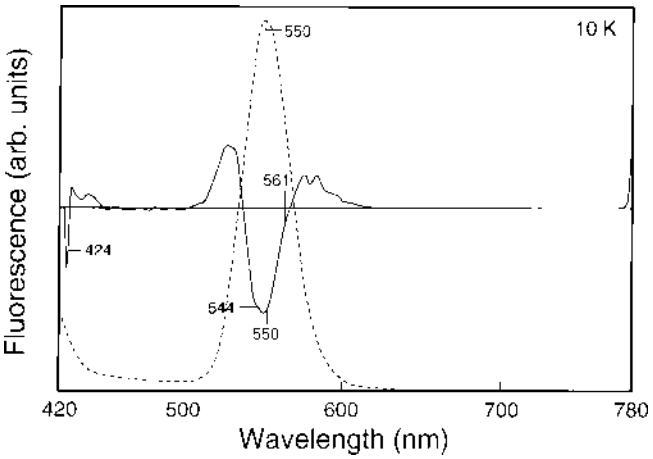

Figure 12. The low-temperature 10.0 ± 0.1 K photoluminescence, no S-defect, tabular-grain $AgBr_{0.88}I_{0.12}$, AgBr core surrounded by AgBr,I shell (optically uncorrected, dashed line). The second-derivative photoluminescence, minimal S-defect, spectrum (solid line).

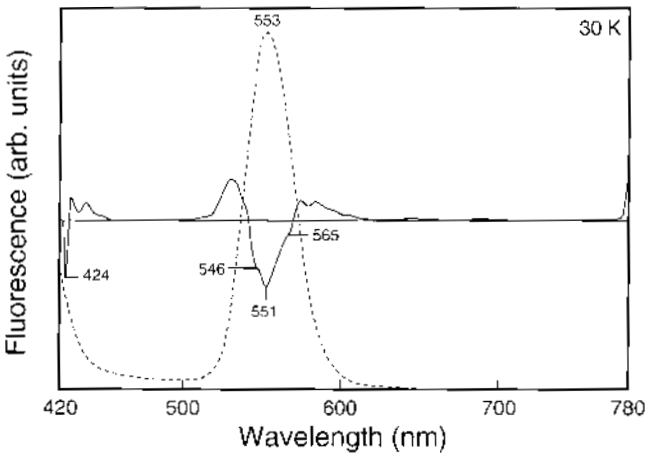

Figure 13. The low-temperature 30.0 ± 0.1 K photoluminescence, minimal S-defect, tabular-grain $AgBr_{0.88}I_{0.12}$, AgBr core surrounded by AgBr,I shell (optically uncorrected, dashed line). The second-derivative photoluminescence, minimal S-defect, spectrum (solid line).

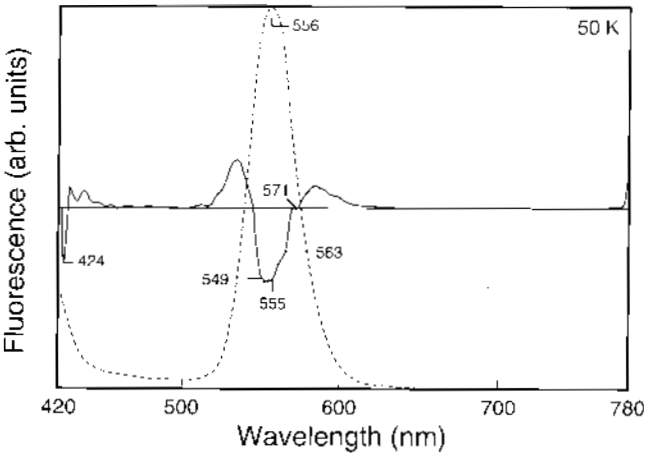

Figure 14. The low-temperature 50.0 ± 0.1 K photoluminescence minimal S-defect tabular grain $AgBr_{0.88}I_{0.12}$, AgBr core surrounded by AgBr,I shell (optically uncorrected, dashed line). The second-derivative photoluminescence, minimal S-defect, spectrum (solid line).

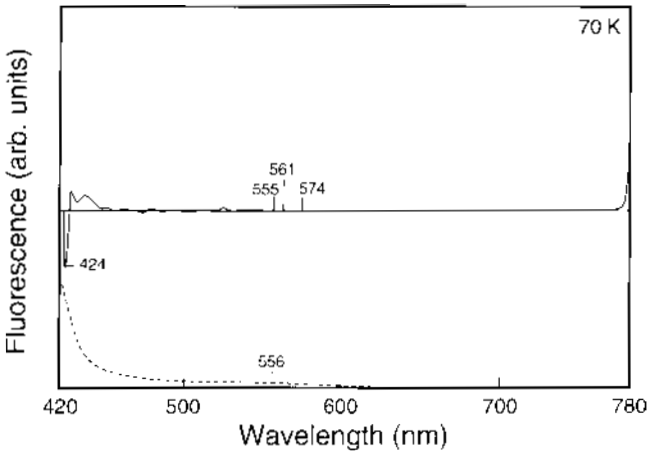

Figure 15. The low-temperature 70.0 ± 0.1 K photoluminescence minimal S-defect tabular grain $AgBr_{0.88}I_{0.12}$, AgBr core surrounded by AgBr,I shell (optically uncorrected, dashed line). The second-derivative photoluminescence, minimal S-defect, spectrum (solid line).

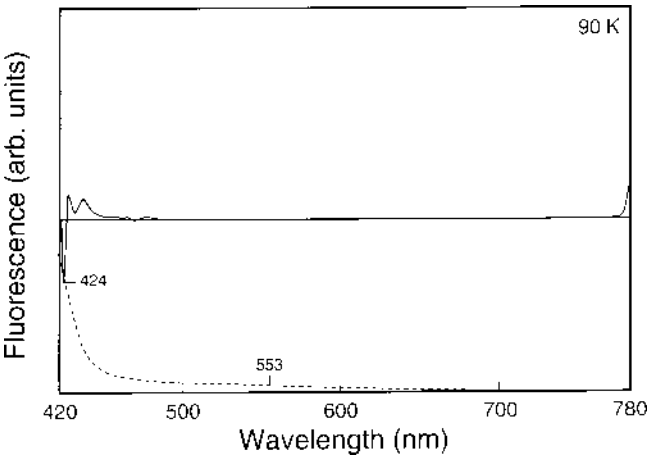

Figure 16. The low-temperature 90.0 ± 0.1 K photoluminescence minimal S-defect tabular-grain $AgBr_{0.88}I_{0.12}$, AgBr core surrounded by AgBr,I shell (optically uncorrected, dashed line). The second-derivative photoluminescence, minimal S-defect, spectrum (solid line).

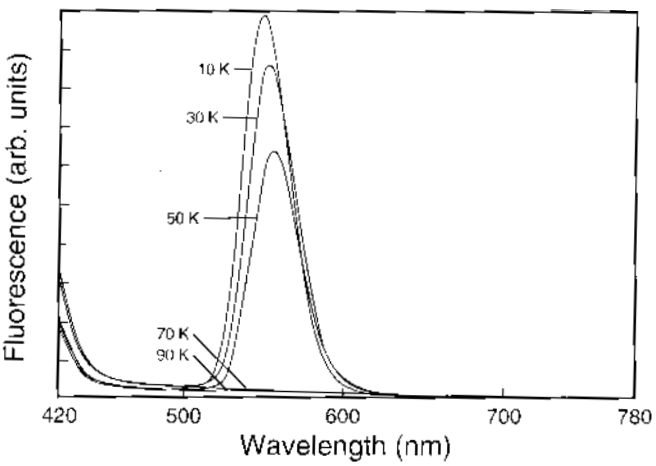

Figure 17. The optically uncorrected, low-temperature 10 to 90 K photoluminescence, minimal S-defect, spectrum of $AgBr_{0.88}I_{0.12}$, tabular-grain 420 to 780 nm with excitation at 400 nm.

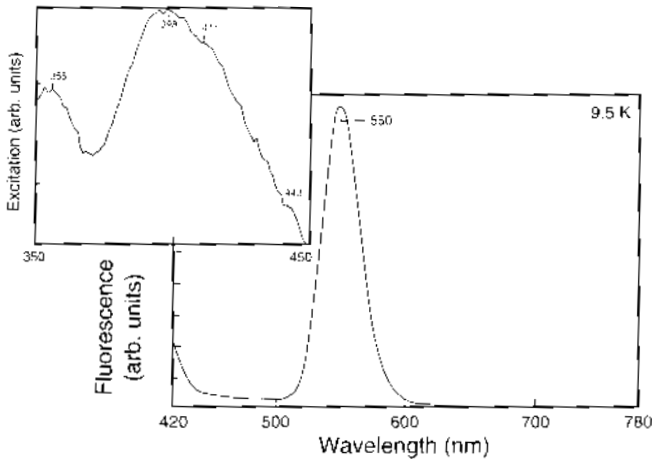

Figure 18. The excitation spectra (Sample 1) 350 to 450 nm, 9.5 K monitored at 550-nm emission. The excitation spectra were similar for 555- and 566-nm emissions.

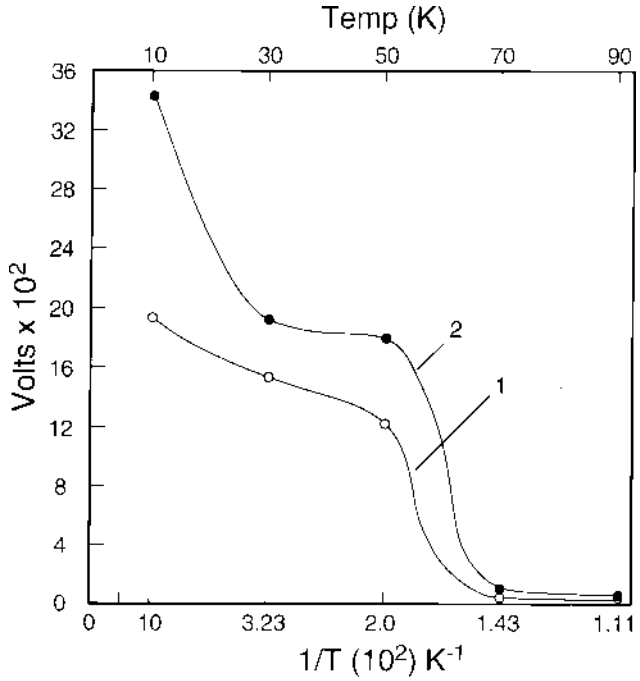

Figure 19. The steady-state peak photoluminescence in vacuum $AgBr_{0.88}I_{0.12}$ S-defect Sample 2 (551 to 556 nm) and minimal S-defect Sample 1 (554 to 560 nm) 10 to 90 K, respectively.

In Sample 2, the S-defect is shown to possess a greater number of emitting defect centers than Sample 1.

Figure 20, the second-derivative peak photoluminescence (signal voltage) of the minimal S-defect, Sample 1, versus temperature ascribes the lower wavelength sensitivity, ~546- and 555-nm components, to quenching processes within the AgBr matrix. The long-wavelength ~562- and 571-nm minor components demonstrate an increasing signal rise, then decline, in the 50 to 90 K region. It is suggested that the R-type, Ag_3°, centers could be formed[1a,b] and the hole mobility caused by temperature rise, increased to cause dissociation of the centers in this region.[29]

Figure 21, again the second-derivative peak photoluminescence of the S-defect, Sample 2 versus temperature, attributes the lower wavelength sensitivity ~549- and 555-nm components, to the quenching processes within the AgBr matrix. The strong difference of the 555-nm signal (30 to

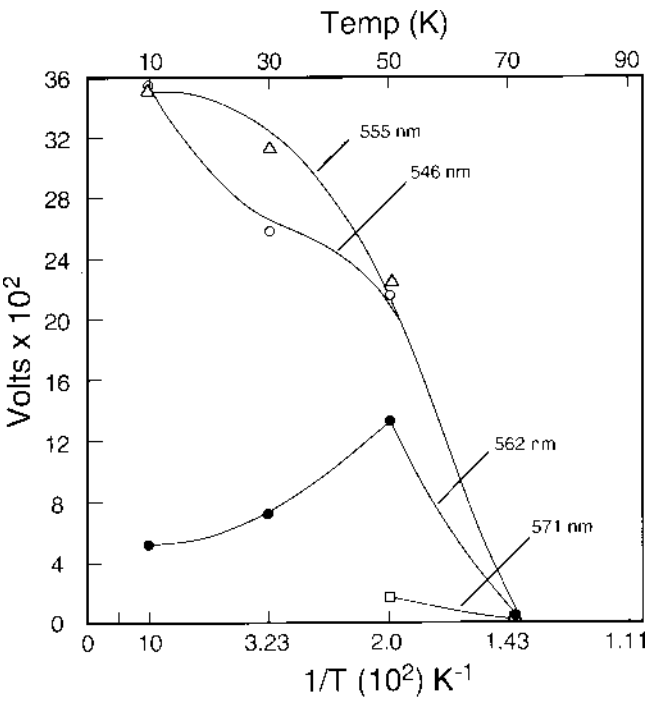

Figure 20. The second-derivative peak photoluminescence of minimal S-defect Sample 1 versus temperature; ○, Δ short-wavelength (549, 555 nm) components and ●, □ long-wavelength (562, 571 nm) components.

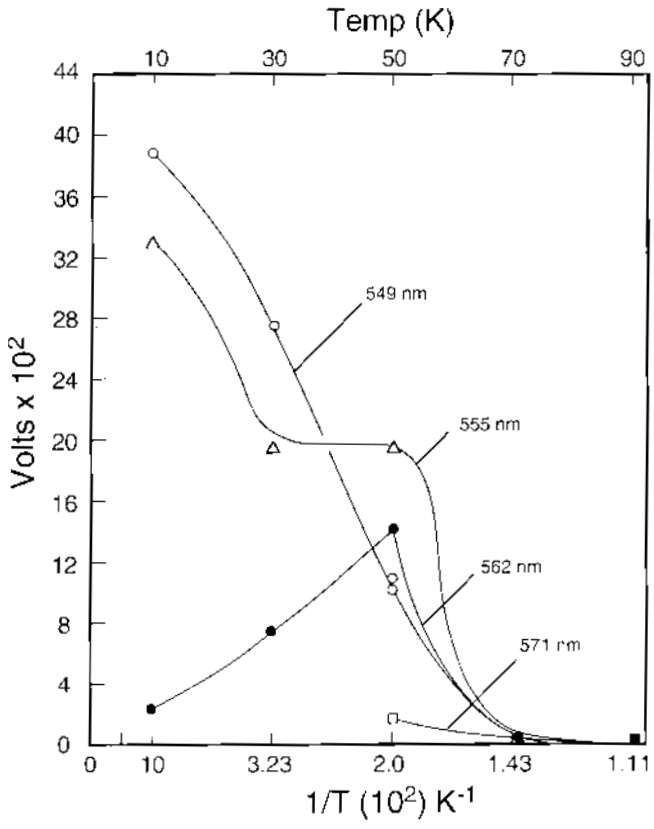

Figure 21. The second-derivative peak photoluminescence of S-defect Sample 2 versus temperature; ○, Δ short-wavelength (549, 555 nm) components and ●, □ long-wavelength (562, 571 nm) components.

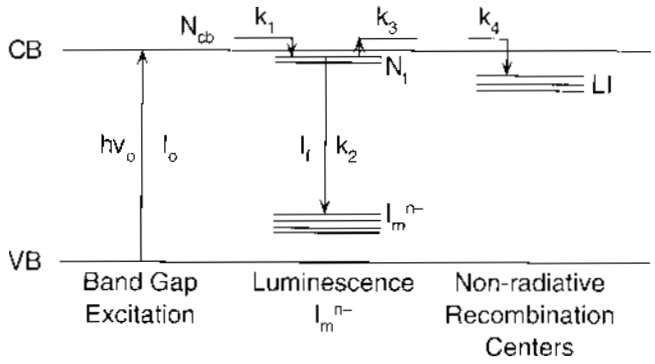

Figure 22. The model for iodide photoluminescence.

50 K) for the S-defect reflects a greater intensity, number density, and shallower recombination centers than Sample 1. This difference could be related to the bulk defects in the double-twin plane leading to the surface features. The electron-trapping characteristics of the 549-nm center of Sample 2 are similar to the 555-nm center of Sample 1.

The results cited may be interpreted as shallow centers represented by electron traps.[30] In addition, electrons are irreversibly removed from the conduction band by deep traps or emitting recombination centers. The following are defined in the proposed model shown in Fig. 22: k_1 is capture probability by shallow trapping center, k_2 is radiative recombination probability at the iodide emitting centers (after activation energy to the conduction band); k_3 is the thermal activation probability to the conduction band from shallow trapping centers; k_4 is probability for irreversible removal from the conduction band by nonradiative processes; N_{cb} is the number of electrons in the conduction band; N_t is the number of electrons in shallow trapping centers leading to luminescence or recombination and thermal activation; LI is the latent image, and the steady-state photoluminescence efficiency is derived[31] (Fig. 22) by

$$\varnothing = k_2 N_t / I_0 = \left[1 + \left(k_4/k_1\right) + \left(k_3 k_4 / k_1 k_2\right)\right]^{-1}, \qquad (1)$$

where I_0 is the rate of excitation. It is assumed that all processes are first order, and the number of traps is large compared to N_{cb}.

The probability k_3 is the rate determining, slow step and assumed to be determined according to $k_3 = A\exp\left(-\Delta E_{act}/kT\right)$, where A is of the order of the lattice vibrational frequency and ΔE is the trap depth. When $k_1 \gg k_4$, Eq. 1 reduces the thermally quenched luminescence.[30] Hole transport and other shallow trapping have been neglected.

The decrease of nonradiative processes, k_4, filling of some of the deep traps that determine k_4 in low-intensity measurements, moves the onset of the photoluminescence decrease to higher temperatures (Figs. 20 and 21). This phenomenon is due to increased recapture of electrons at the trapping centers of N_t.[30,31] Thus, in Sample 2 versus Sample 1 the filled centers involving k_4 are more numerous, therefore, the luminescence is more pronounced and extended in Fig. 21, 70 to 90 K compared to Fig. 20. The high luminescence efficiency requires high capture probability of both hole and electron.[1b] Therefore, it appears likely that the hole trap responsible for the short-hole [Fig. 23(a) and 23(b)] lifetimes predicted may be identified with the recombination center of the iodide cluster.[1b] The nature of the recombination center has been described.[1b]

Mechanisms of Iodide Luminescence.[1b] Figures 23(a) and 23(b) represent the structures and mechanisms involving the luminescent iodide centers in silver halide. The energy state diagram (1) provides a mechanism for the analysis of the photophysics; i.e., the radiative and radiationless processes that correspond to electronic transitions between the states without introducing Frenkel disorder relating to point defects; and (2) relates to Frenkel disorder.

In Fig. 23(a), the highest occupied level, HOMO, of the iodide species, transfers an electron to the valence-band hole subsequent to excitation, thus injecting a hole into the iodide sites, where electron recombination emission is detected in direct competition with latent-image formation or sulfide trapping centers, however, at room temperature, the iodide center becomes more of a hole trap than a recombination center. The limitation of this recombination mechanism is the rate of transfer of the iodide (cluster m, n, and o) HOMO electrons to the valence-band hole. The rate must be greater than the rate of electron recombination with the hole at the iodide site, i.e., $2 > 1 > 3$. If $1 \geq 3$ then image formation becomes inefficient, and if $1 < 3$ then latent-image formation is diminished by the ratio of the rate constants k_1/k_3.

Figure 23(b) describes an alternative low-probability mechanism[32,33] relating a positive charge site for the iodide-

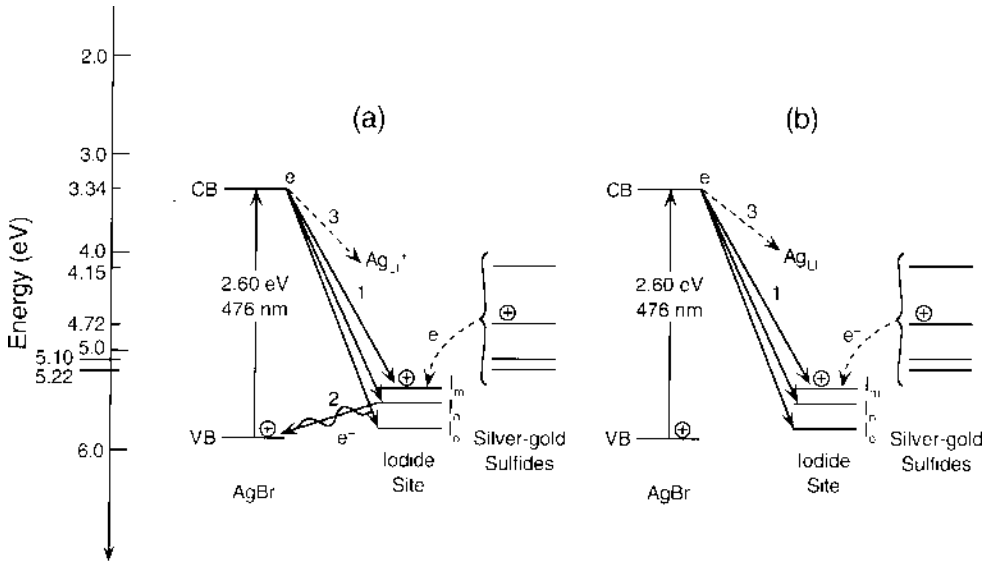

Figure 23. (a) Electronic structures and mechanisms involving the luminescence iodide centers in silver bromide without introduction of Frenkel disorder. (b) Photochemical model of luminescence iodide centers with relation to Frenkel point defects: CB, conduction band; VB, valence band.

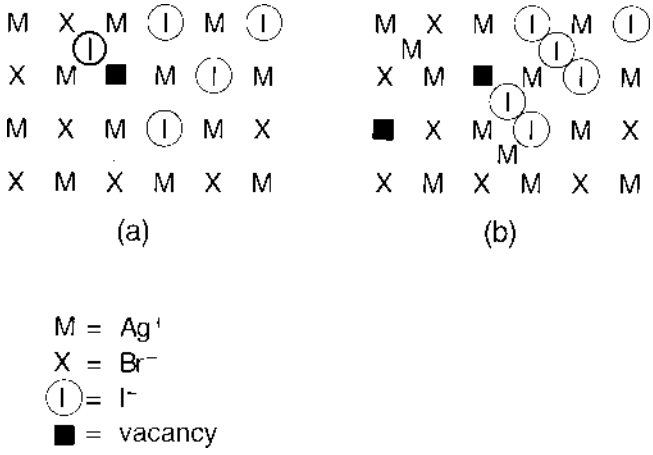

Figure 24. (a) Frenkel disorder on the halide sublattice with substitutional iodide site. (b) Frenkel disorder on the halide sublattice with substitutional iodide and interstitial placement, cluster or domain grouping of iodide anions.

recombination cluster emission in terms of Frenkel disorder on the halide sublattice (e.g., equal number of vacancies in the halide sublattice and in the halide interstitial ions). This configuration may lead to a high-energy strained crystal arrangement because of the size of the iodide ion. The more probable mechanism would involve the defect iodide associated with the interstitial silver ion.

As shown in Fig. 23(b), the iodide clusters are competing with the conduction-band electrons subsequent to excitation to form the latent-image center. Again the latent-image rate of formation must be greater than the recombination emission at the iodide aggregate for efficient imaging, i.e., $3 \geq 1$; when $1 > 3$, the photographic efficiency may be diminished by the ratio of k_1/k_3.

The substitutional, Fig. 24(a) (540 nm), and interstitial, Fig. 24(b) (590 nm), disorder configurations may be the short- and long-wavelength emissions, respectively, depending on the size and conformation of the clusters of the iodide atoms.

In summary, the electron is attracted to the Coulombic iodide as a recombination center because of a relative positive charge induced by a photokinetic hole injection to the iodide cluster or nearest-neighbor anion vacancy, Fig. 23(a), or the much more probable silver ion interstitial, Fig. 23(b), the silver interstitial ion not shown. The recombination emission is not that of AgI pure crystal, but of iodide clusters in a defect lattice.

In the case of the bromo-iodides, the positive holes are trapped at the sites of the iodide ions (complexes of lattice structures) to form bound excitons after electron capture, and subsequent emission. Thus, the excited system returns to the ground state also by transferring to a high vibrational level of the ground state from which it may gradually return with the transfer of energy to the lattice.

The electron transfer process may also involve R-type formation as shown by the second-derivative spectra of both Sample 2 and Sample 1 at 571 nm.[1a] The activation energy ΔE to the conduction band (k_3 seen in Eq. 1) may be provided by the vibrational activation of the crystallites at higher temperatures where a higher competition exists between the dissipation processes and photoluminescence. At very low temperatures only fluorescence occurs. A simplified derivation using Fig. 22 is instructive.[15] If R is the photoluminescence process in terms of the probability/s, and NR the nonradiative crystal vibrational dissipation process, the quantum efficiency of fluorescence is given by the following[15]:

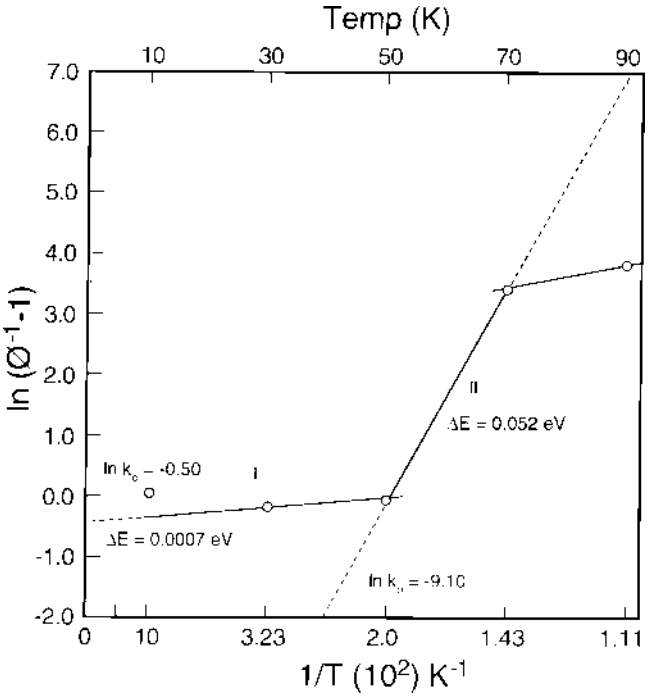

Figure 25. A plot of $\ln(Ø^{-1}–1)$ versus $1/T$; Ø, the quantum efficiency against the reciprocal temperature for Sample 2, S-defect microcrystallites $AgBr_{0.88}I_{0.12}$. (○ represents the major peak photoluminescence signal at 544 nm.)

$$\varnothing = \frac{R}{R+NR} = \frac{1}{1+\dfrac{NR}{R}} = \frac{1}{\left[1+K_o \exp\left(\dfrac{-\Delta E_{act}}{kT}\right)\right]} \qquad (2)$$

The fraction NR/R contains the Boltzmann factor $A \exp(-\Delta E_{act}/kT)$, where A is the vibrational frequency (60 K:$1.23 \times 10^{+12} s^{-1}$) of the system in the excited state and the entropy contribution is considered negligible, k is the Boltzmann constant, and T is the absolute temperature. A transfer coefficient t has values of 0 to 1 to account for the electron probability of returning to the conduction band and subsequently to the recombination center. The variable K_o is defined as tA/R without the entropy terms $\exp(\Delta S^{+}_{act}/k)$ for NR and R components. Thus, a comparison to experiment with a transformation of Eq. 2 is

$$\ln\left(\varnothing^{-1}-1\right) = \ln K_o - \frac{\Delta E_{act}}{kT}. \qquad (3)$$

Therefore, a plot of $\ln(Ø^{-1}–1)$ versus $1/T$ should yield a straight line, the slope of which gives $-\Delta E_{act}/k$ and whose intercept with the $\ln(Ø^{-1}–1)$ axis yields $\ln K_o$. The E_{act} energy reflects the shallow electron trap energy beneath the conduction band.

The fundamental data of Figs. 4 through 8 and Figs. 12 through 16 with the accompanying second-derivative spectra yield a plot of the quantum efficiency against temperature. The initial low-temperature invariant part of the curve represent Ø = 1. All the curves, Sample 2 versus Sample 1, reference the highest signal as Ø = 1; i.e., Sample 2 (10 K).

For Sample 2, the nonderivative (Fig. 25) values of Ø range from 1.00 to 0.534 and for $\ln(Ø^{-1}–1)_o$ from $(\ln K_o)$ –0.50 to –9.10 extrapolated at 0 to 50 K also for values of Ø ranging from 0.534 to 0.0331 and for $\ln(Ø^{-1}–1)_o$ from $(\ln K_o)$ –9.10 to +2.0 with temperatures 50 to 70 K $[(1/T)(100)K^{-1}$ from 2.0 to 1.43]. (ΔE_{act} = 0.0007, 0.052, and

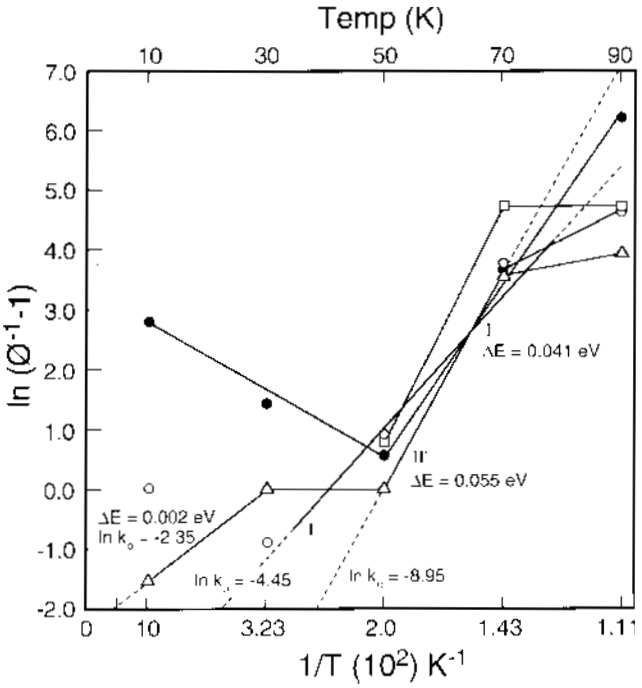

Figure 26. A plot of $\ln(Ø^{-1}–1)$ versus $1/T$; Ø, the quantum efficiency of the second-derivative against reciprocal temperature for Sample 2, S-defect microcrystallites $AgBr_{0.88}I_{0.12}$. The ○ and Δ represent the 549- and 555-nm major bands whereas the ● and □ represent the 562- and 571-nm minor bands.

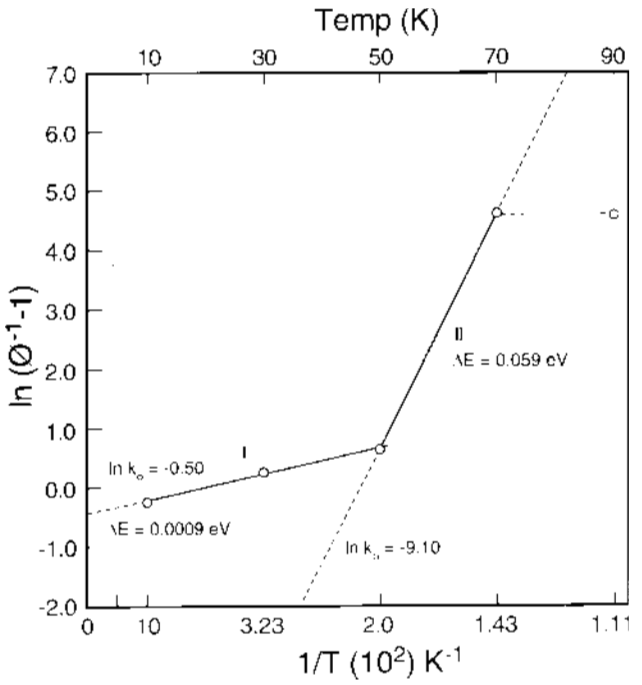

Figure 27. A plot of $\ln(Ø^{-1}–1)$ versus $1/T$; Ø, the quantum efficiency against reciprocal temperature for Sample 1, referenced with Sample 2 maximum signal. (○ represents the major peak photoluminescence signal at 550 nm.)

0.0105 eV for 0 to 50, 50 to 70, and 70 to 90 K temperature ranges).

Above 50 K, deviation from linearity is appreciable and is noted by the long-wavelength resolved bands of 562 and 571 nm attributed to unstable photoluminescence from silver Ag_3° clusters.[1a] This mechanism is shown by Fig. 26, wherein the curve for 562 and 571 nm is the reciprocal trace of Figs. 20 and 21.

The linear extrapolation to higher temperatures predicts lower quantum efficiencies than actually observed; e.g., 1.0×10^{-3} theoretical versus 2.3×10^{-2} observed at 90 K for Sample 2 (Fig. 26).

The values of ΔE_{act} derived from the straight line plot (nonderivative data) for the S-defect and the minimal defect are 0.052 eV (Fig. 25) and 0.059 eV (Fig. 27), respectively, which describe a shallow electron trap Fig. 22 beneath the conduction band. Note that a smaller activation energy provides higher quantum photoluminescence efficiency; i.e., Sample 2. The derivative ΔE_{act} is slightly higher for both S-defect and minimal defect; 0.055 (Fig. 26) and 0.065 eV (Fig. 28), accordingly. Thermal energy for a 50 K electron is 0.00431 eV, therefore, the shallow trap requires approximately 13.6 times this energy to detrap an electron at these temperatures. The nonradiative dissipation energy is provided from the vibrational relaxation of the crystallite. (Thermal energy for 10, 30, 50, and 90 K is 0.000862, 0.00255, 0.00431, and 0.00778 eV, respectively.)

We assumed that ΔE_{act} was independent of temperature. Because the lattice vibrations are a function of temperature, they are also a function of the equilibrium configuration of the ions and the substitutional dopants such as iodide ions. Then ΔE_{act} should be expressed accordingly as a function of temperature and should take the form of a polynomial expansion similar to the heat capacity; i.e., $\Delta E = \Delta E_o + \alpha T + \beta T^2$, where ΔE_o is the value ΔE at absolute zero.

The ratio of NR/R is related in a more complex relationship than presented in Eq. 3. (Ref. 15) The preexponential term should also include the entropy terms. The assumption

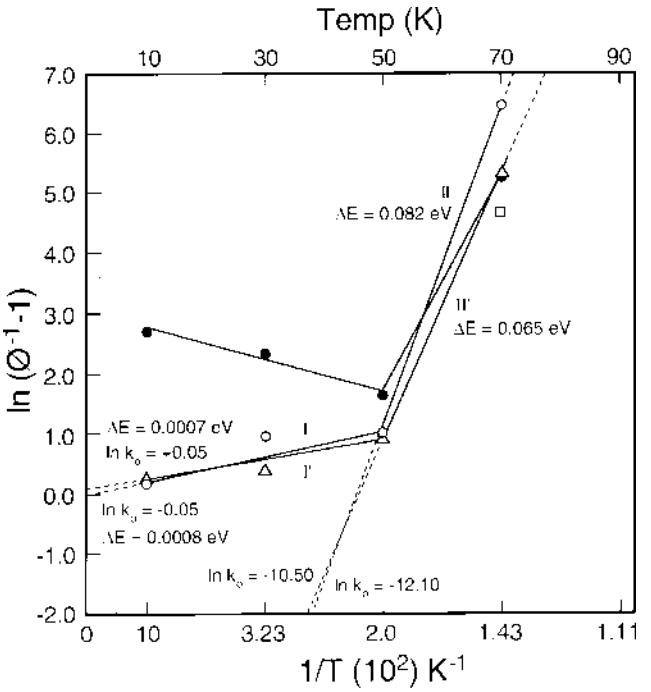

Figure 28. A plot of $\ln(Ø^{-1}–1)$ versus $1/T$; Ø, the quantum efficiency of the second-derivative against reciprocal temperature for Sample 1, reference with Sample 2 maximum signal. (The ○ and Δ represent the 546- and 555-nm major bands whereas the ● and □ represent the 565- and 571-nm minor bands.)

that the transmission coefficient is equal to 1 is a simplified construct also there is the omission of a tunneling factor.[34]

Photoluminescence and the Relationship to Iodide Cluster Diameter. Figure 29 shows the energy of the lowest excited electronic state (i.e., the conduction band plus the transition recombination energy at the peak

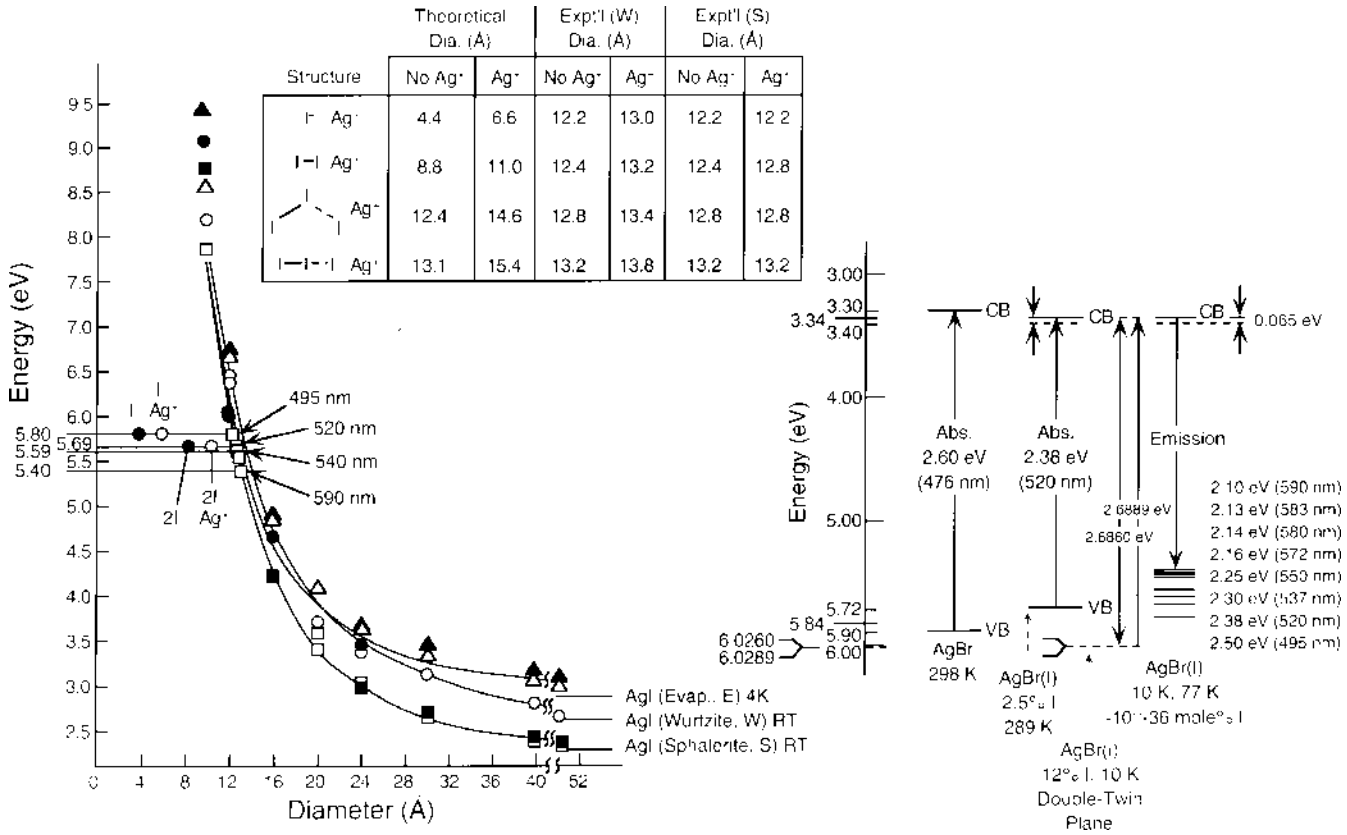

Figure 29. The correlation of the transition recombination energy at peak photoluminescence wavelength versus iodide cluster diameter. The Δ, ○, and □ and ▲, ●, and ■ indicate band-gap values 2.93, 2.63, and 2.22 eV with estimated effective electrons $m^*_{e^-}$ (0.286), (0.286) and the effective holes $m^*_{\hbar^+}$ (1.096), (0.60) paired, respectively, and the optical frequency dielectric $\in$ = 5.419 (500 nm).

photoluminescence wavelength versus the small iodide cluster diameter). These curves, derived from Eq. 4, are used to determine the iodide cluster size.[32,33,35–40]

The theory relates the size of small clusters to quantized energy levels. The spacing between the adjacent states being of the order E_f/N, where E_f is the Fermi energy and N is the number of atoms in a cluster. Because E_f has a value of a few electron volts, the energy levels in a cluster of $10^{+3} - 10^{+1}$ atoms are separated by about $10^{-3} - 10^{-1}$ eV, as seen in Fig. 29 for photoluminescence of iodide centers. The particle-in-a-box theory presented previously[1a,b] is applied but with inclusion of the Ag^+ within the AgBr matrix. Allowance was made in Fig. 29 for the $Ag^+ - I^-$ bonding. The optical frequency dielectric[36,41] for AgI (486 nm) $\in$ = 5.419 is inserted in the Coulomb attraction term and the third-solvation energy-loss term is not applicable.[1a,b,c] The effective masses $m^*_{e^-}, m^*_{\hbar^+}$ of electrons and holes are approximated from literature values by comparing semiconductor properties.[42,43] Silver bromide effective masses have been used as reference. In terms of an overlap model,

$$\mathrm{Eg}(R) = \mathrm{Eg}(R=\infty) + \frac{\hbar^2\pi^2}{2R^2}\left[\frac{1}{m^*_{e^-}} + \frac{1}{m^*_{\hbar^+}}\right] - \frac{1.8e^2}{\in R} + \frac{e^2}{R}\sum_{n-1}^{\infty}\alpha_n\left(\frac{S}{R}\right)^{2n}, \quad (4)$$

the larger the overlap of holes and electrons between different atoms or ions, the wider the band state becomes; the wider this band, the smaller the effective mass. The effective electrons $m^*_{e^-}$ (0.286), (0.286) and the effective holes $m^*_{\hbar^+}$ (1.096), (0.60) paired, respectively, for two trial calculations are shown in the second confinement energy term for the allotropic forms of AgI. The value Eg($R = \infty$) is taken as a reference energy at room temperature of the βAgI wurtzite band gap (2.63 eV) and of the (2.22 eV) band gap of sphalerite, γAgI. The value Eg(R) is the recombination emission to states representing the quantum size (R) radius of the iodide aggregates. An evaporated film of 2.92-eV band gap at 4 K is also considered with each of the paired effective masses for holes and electrons. The emission spectra are quite different from those for bulk material relating the different structures of iodide within the AgBr lattice.

The 540-nm region represents a suggested bent I_3^- anion, or $(AgI_3)_n$, assuming a theoretical diameter of 14.6 Å (12.4 Å without Ag^+) as the long axis of the triangle versus 13.4 Å for wurtzite and 12.8 Å for sphalerite calculated diameters (including Ag^+ bond) observed from the emission-spectroscopic-curve analysis (Fig. 22). The calculated confinement volume of the exciton is 1259 $Å^3$ (W) and 1098 $Å^3$ (S) for the bent iodide. Cubic sphalerite 4 mols/unit lattice has a unit cell volume of 273.89 $Å^3$, which yields 64 ats./cluster or 16 mol./cluster $(2I - {}^-IAg^+)_n$. The wurtzite hexagonal 2 mol./unit lattice structure has a unit cell volume of 137.2 $Å^3$, which yields 72 ats./cluster or 18 mol./cluster.

The 590-nm-region emission not present here but observed in previous studies[1a,b] related to a linear structure of 13.8 Å (W) diam versus 13.2 Å (S) for wurtzite and sphalerite allotropic forms, respectively. Again, the calculated confinement volume of the exciton is 1376.1 $Å^3$ (W) and 1204.3 $Å^3$ (S) for the 4 at. (3 iodide, 1 silver) linear molecules and yields 20 mols/cluster or 80 ats./cluster for hexagonal wurtzite structure. The cubic sphalerite form approximates 18 mols/cluster or 72 ats/cluster for the linear arranged clusters. Longer wavelength bands, overlapping the 562 to 571 nm unstable Ag_3° emissions,[1a,b] are

TABLE I. Experimental Electronic Photoluminescence Energy Levels Used in the Determination of I_3^- Cluster Size in AgBr,I Utilizing Eq. 4

Expt. *E* (R) eV (AgBr C.B. 3.30 eV)			Diameter (Å) I_m^{n-} Cluster	$Ag^+ - I_m^{n-}$ Theoretical	Calculated+ Ag^+ (W)	Calculated+ Ag^+ (S)	I_n^- Atoms cluster + Ag^+ (W)	I_n^- Atoms cluster + Ag^+ (S)	Molecules I_n^-/cluster + Ag^+ (W)	Molecules I_n^-/cluster + Ag^+ (S)
495 nm	(5.80)	1 at.	4.4	6.6	13.0	12.2				
520 nm	(5.69)	2 at.	8.8	11.0	13.2	12.6				
540 nm	(5.59)	Bent	12.4	14.6	13.4	12.8	72	64	18	16
590 nm	(5.40)	Linear	13.1	15.4	13.8	13.2	80	72	20	18

(S), sphalerite, cubic unit cell length 6.4942 Å. (W), wurtzite, hexagonal unit cell length 4.5930 Å.

interpreted as larger clusters of I_m^{n-} in the presence of Ag^+. I_m^{n-}These structures emit radiation not as AgI, but as larger domains of iodide near silver centers in the AgBr lattice. A deviation is seen (Fig. 29) for the 520-nm 2-at. iodide molecule exciton,[9,13] the diameter of which should be 8.76 Å, I–I or 11.0 Å I–I$^-$Ag$^+$ versus the experimentally (spectroscopic energy versus diameter graph) calculated diameter of 13.2 Å. A deviation is also seen for the 1-at.-diam iodide center, calculated 4.4 Å, I^-, or I^- Ag^+ 6.6 Å (Eq. 4) (Refs. 9 and 13). A summary of the data is shown in Table I. Can quantum clusters of such small magnitudes possess cubic or hexagonal symmetry? Note in Fig. 29 the curves (symmetry) converge at small radii.

The HOMO, hole-trapping species of the iodide center, has been observed by the photoluminescence; the LUMO, lowest unoccupied molecular orbital, for the iodide electron trapping (NS) center is 0.065 eV beneath the conduction band whereas the (S) electron trapping center is 0.055 eV beneath the conduction band. We conclude that the emission assignments take into consideration these shallow electron traps at room temperature (Figs. 29 and 30).

Figure 30 summarizes the proposed energy levels of Ag_2S, Ag_3AuS_2, AgAuS, iodide, and $Ag^\circ_m Ag^+_i$ clusters relative to AgBr.[1a,b,5]

Photoluminescence and Excitation Spectra of Double-Twinned Microcrystals. The excitation spectrum of Sample 2, Fig. 31, was obtained when the monitoring wavelength was 554 nm (the recombination emission of small iodide quantum clusters).[1a,b] A high-energy band is shown at 456.5 and 457.0 nm. Figure 32, the emission spectrum, with second-derivative excitation at 443 nm was compared with the second-derivative excitation in Fig. 33. The higher energy excitation (dashed) is shown at 461.0 nm (2.6889 eV), the assigned indirect exciton band gap, and the exciton localization at the twin plane is 461.5 nm (2.6860 eV). [The excitation band at 456.5 nm (2.715 eV) is the position of the absorption maximum and is slightly larger than that of the indirect exciton gap.][29a] The splitting in the excitation spectrum of the double-twin-plane microcrystal is 2.9 meV. The assigned 0–0 band of the iodide bound exciton I_{oo} is positioned at 469.5 nm (2.6402 eV).[44] Excitation spectra in the literature were also obtained on octahedral microcrystal dispersions, 6 K, without the prominent new band attributed to the twin plane. Note the surprising absence of the exciton band-gap energy [Eg (ex) = 2.6838 eV, 461.88 nm] for both the single twin and the octahedral spectra within the excitation spectra.[44] Figures 34 through 36, Sample 1, have similar attributed features of Sample 2; e.g., 461.0 nm (2.6889 eV) indirect exciton gap (dashed) Fig. 34, excitation spectrum and the lower energy exciton localization at the double-twin plane 461.5 nm (2.6860 eV); i.e., 2.9 meV. Figure 35,

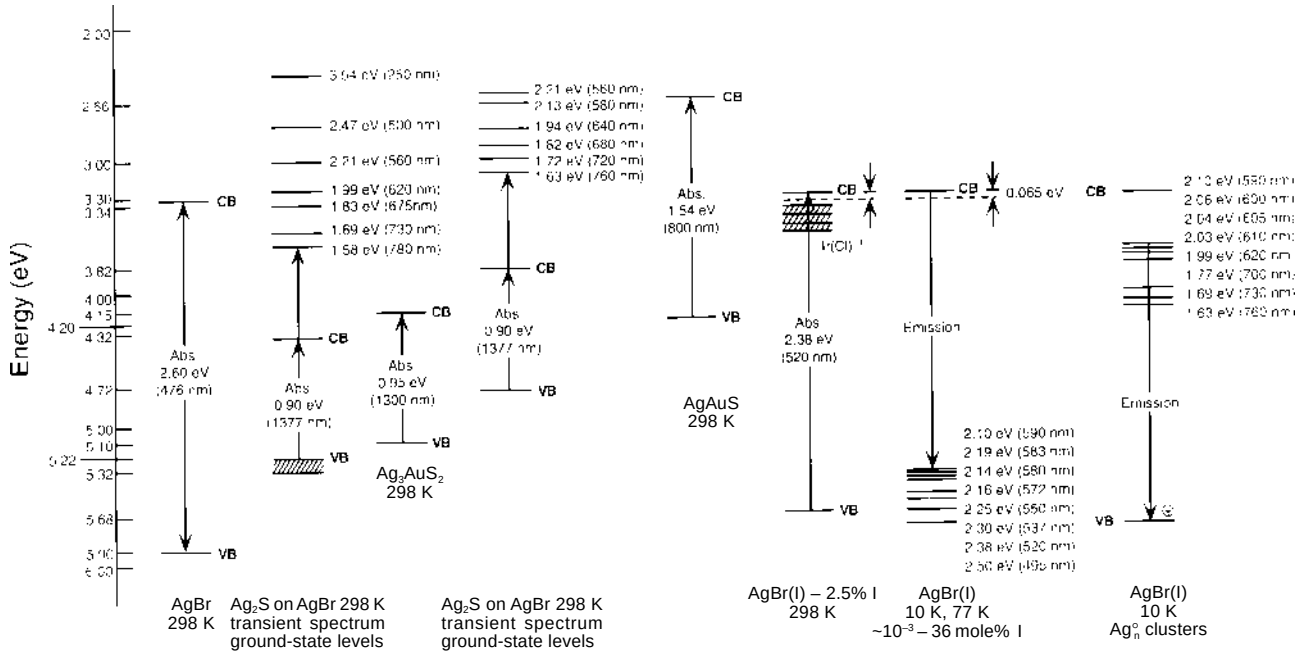

Figure 30. A summary of energy levels of Ag_2S, Ag_3AuS_2, AgAuS, iodide, and $Ag^\circ_m Ag^+_i$ clusters relative to AgBr: CB, conduction band; VB, valence band.

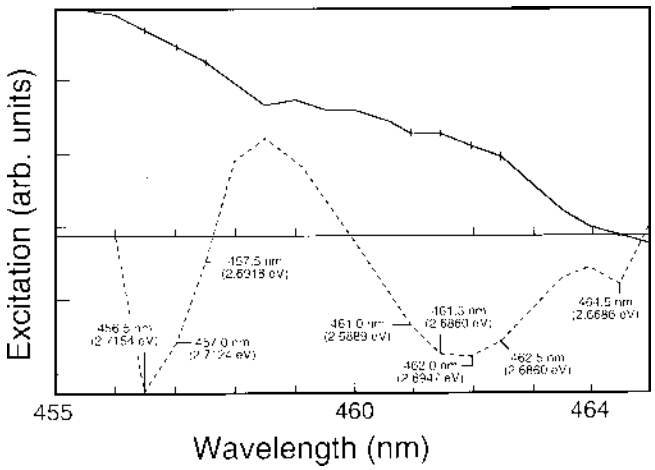

Figure 31. Excitation (solid line) and second-derivative (dashed line) spectra of double-twinned $AgBr_{0.88}I_{0.12}$ (S-defect, Sample 2) microcrystals at 10 K. The monitored wavelength was 554 nm.

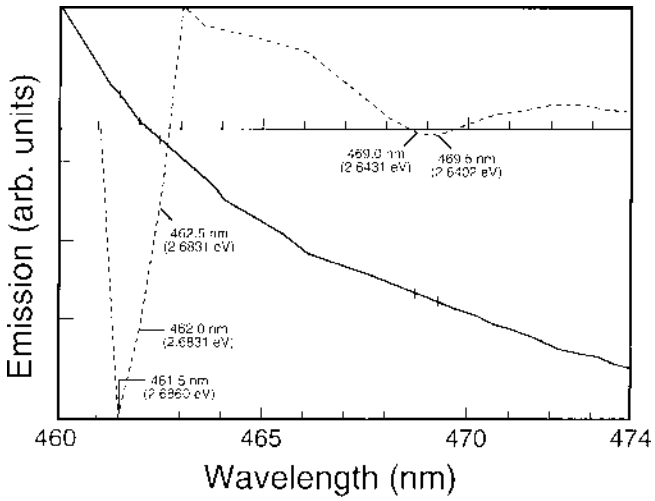

Figure 32. Emission (solid line) and second-derivative (dashed line) spectra of double-twinned $AgBr_{0.88}I_{0.12}$ (S-defect, Sample 2) microcrystals at 10 K. The exciting wavelength was 443 nm.

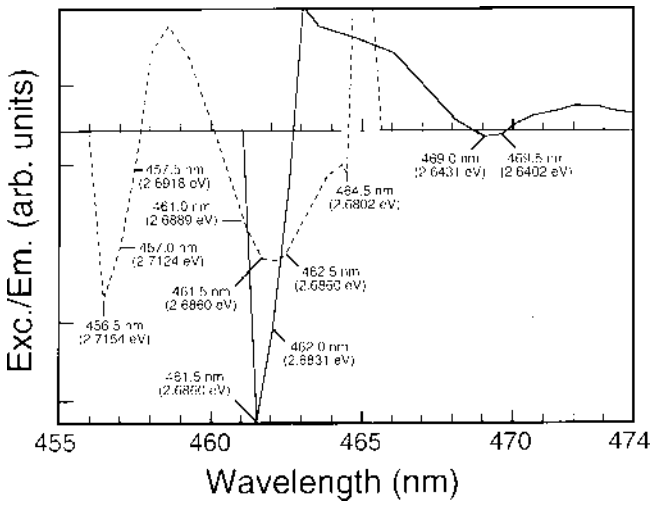

Figure 33. The excitation (dashed line) and emission (solid line) spectra are compared. The higher energy excitation is 461.0 nm (2.6889 eV), the indirect exciton gap, and the exciton localization at the twin plane is 461.5 nm (2.6860 eV). The splitting in the excitation spectrum of the double-twin-plane microcrystal is 2.9 meV. The assigned o-o band of the iodide-bound exciton I_{oo} is 469.5 nm (2.6402 eV).

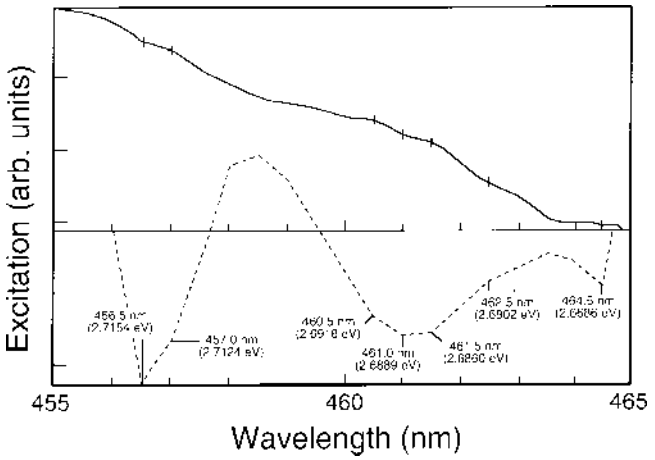

Figure 34. Excitation (solid line) and second-derivative (dashed line) spectra of double-twinned $AgBr_{0.88}I_{0.12}$ (minimal defect, Sample 1) microcrystals at 10 K. The monitored wavelength was 554 nm.

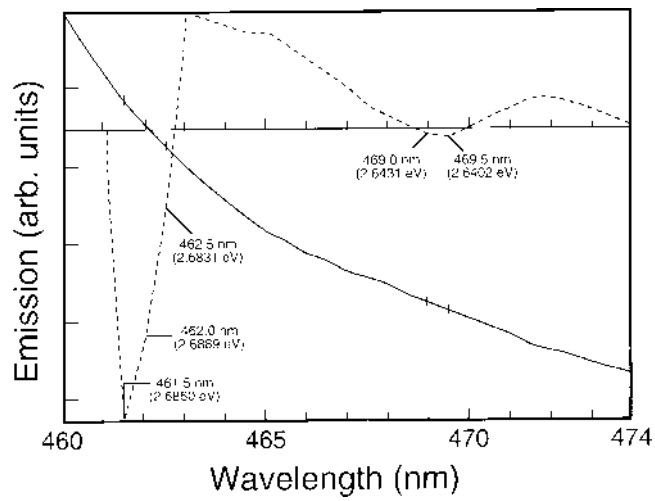

Figure 35. Emission (solid line) and second-derivative (dashed line) spectra of double-twinned $AgBr_{0.88}I_{0.12}$ (minimal defect, Sample 1) microcrystals at 10 K. The exciting wavelength was 443 nm.

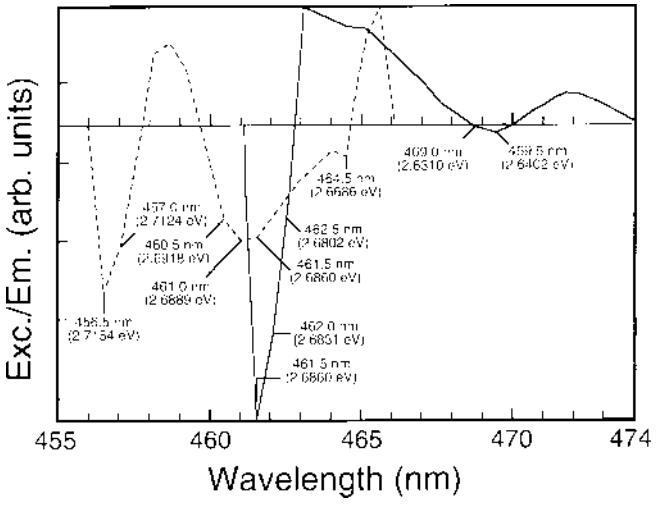

Figure 36. The excitation (dashed line) and emission (solid line) spectra are compared. The higher energy excitation is 461.0 nm (2.6889 eV), the indirect exciton gap, and the exciton localization at the twin plane is 461.5 nm (2.6860 eV). The splitting in the excitation spectrum of the double-twin-plane microcrystals is 2.9 meV. The assigned o-o band of the iodide-bound exciton I_{oo} is 469.5 nm (2.6402 eV).

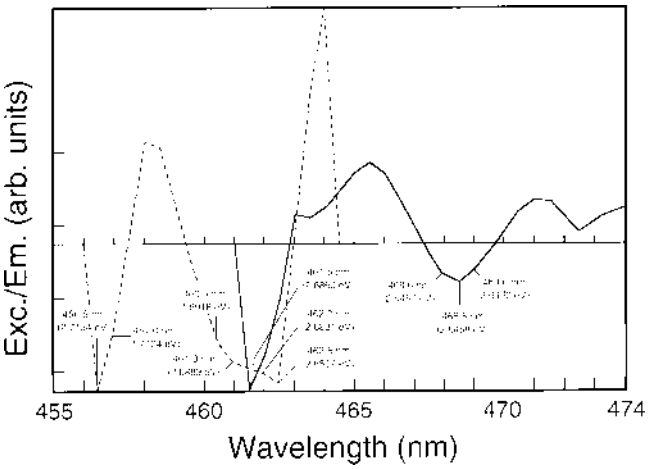

Figure 37. The excitation (dashed line) and emission (solid line) second-derivative spectra are compared for a 0.35-μm cubic microcrystal dispersion of AgBr (97.4%)–I (2.6%) without twin planes.

the emission spectrum, shows the 469.5 nm, I_{∞}-bound iodide exciton and the 461.5-nm emission from the double-twin plane. Again, a high-energy band centered at 456.5 nm is present in the excitation spectra of Figs. 34 and 36.

From the energy position of the zero-phonon line (2.6402 eV) 469.5 nm, iodide-bound exciton, relative to the indirect exciton gap energy (2.6889 eV) 461.0 nm,[45,46] the localization energy of the iodide bound state is calculated to be E_i = 48.7 meV. This quantity comprises the binding energy of the hole to the iodine and of the electron to the trapped hole minus the free exciton binding energy. This state is exceptionally stable, relative to the thermal energy at 10 K (0.862 meV). The preexponential, $2.05 \times 10^{+11} s^{-1}$ produces a calculated rate constant of 5.96×10^{-14} or a lifetime of $1.67 \times 10^{+13}$s.

The major feature for both Sample 2 and Sample 1 is the coincident excitation and emission wavelengths at 461.5 nm (2.6860 eV) attributed to the double-twin plane, 93.3 and 100 Å separation, respectively, compared to the higher band-gap energy at 461.0 nm (2.6889 eV). The samples shown in Figs. 33 and 36 exhibit an apparent equivalent doublet in their excitation spectrum with a splitting of 2.9 meV. The tabular microcrystals with double-twin planes of iodide in AgBr are assigned to tunneling of an exciton between the parallel planes.[44] The calculated energy values of a particle in square wells of 93.3 and 100 Å size are 45.3 and 39.4 meV with transition of n = 1 to n = 2. The 2.9-meV experiment splitting data correspond to the hole (m^*_h = 1.096), and electron (m^*_e = 0.286) transit distances of approximately 188 Å and 368 Å, respectively, for both Sample 2 and Sample 1 on excitation. Therefore, we may conclude that both hole and electron could traverse the 93.3- and 100-Å plane separations.[45,46] The stacking-fault-related absorption (excitation spectra) by monitoring the recombination emission at 550 to 554 nm, nano-clusters of iodide anions,[47] suggests these excitons are mobile and migrate from the twin plane. The binding energy would be 2.9 meV as noted by the excitation spectrum. Utilizing this energy and a calculated (10 K = 0.862 meV) preexponential of $2.05 \times 10^{+11}$ s^{-1} yields an estimated rate constant of $7.09 \times 10^{+9}$ s^{-1} or a lifetime of 1.41×10^{-10} s for the hole formed by the absorption during excitation at the twin plane at 10 K.

Note that the broad excitation band may possess an additional band at 462.0 nm (2.6831 eV), Figs. 32 and 36, corresponding to the apparent coincident emission band possibly due to iodide anions in the double-twin plane.

The 0.356-μm cubic microcrystal dispersion of AgBr (97.4%)–I (2.6%), Fig. 37, exhibits a second-derivative photoluminescence excitation spectrum monitored at 530 nm, the iodide-bound exciton emission (dashed line), and is compared with the emission spectrum when the exciting wavelength was 443 nm (solid line). The cubic microcrystal dispersion does not possess a single or double-twin plane; therefore, no coincident excitation and emission wavelengths at 461.5 nm (2.6860 eV) are attributed to the single or double-twin plane. The higher band-gap energy of 461.0 nm (2.6889 eV) is evident in the excitation energy but not seen in the emission spectrum. The 468.5 nm (2.62158 eV) emission spectrum shows the I_{∞}-bound-iodide excition; also present is the 456.5 nm (2.7154 eV) high-energy excitation band.

Conclusions

1. The second-derivative photoluminescence spectra present additional information concerning competing emitting centers not obvious in the steady-state fluorescence spectra; e.g., the added bands of the 562 to 571-nm region of the Ag_3° unstable cluster species[1a,b] show growth and regression between 10 to 90 K.
2. A model is proposed in which the photoluminescence centers are represented by shallow-rate-determining steps: 0.0009 eV (derivative 0.0008 eV) and 0.0007 eV (derivative 0.002 eV) at lower than 30 K extrapolated to 0 K (thermal energy at 10 K is 0.00086 eV and 50 K is 0.0043 eV) and 0.059 eV (derivative 0.065 eV) and 0.052 eV (derivative 0.055 eV) in the 50 to 70 K region for (1) minimal defect and (2) S-defect samples, respectively. The (1) minimal defect and (2) S-defect are 2.6× and 2.2× the thermal energy at room temperature (0.025 eV), respectively. The photoluminescence provides the HOMO or hole-trapping energy at the iodide site, but ΔE provides the LUMO energy levels beneath the conduction band of (1) 0.065 and (2) 0.055 eV, respectively, for the shallow electron-trapping character of these tabular grains.
3. The tabular grain exhibiting striation-like contrast (with three-fold symmetry) parallel to the grain edges and adjacent contrast lines separated by ~0.01 nm (S-defect) has greater quantum efficiency than the grid-like contrast (with one-fold or Pl symmetry) dispersed across the entire grain and these separated from each other by a spacing of 6 ~ 7 nm; e.g., a greater number of the iodide-emitting centers.
4. The large Stokes' shifts of the emission bands that exist for homogeneous run-iodide dispersions of AgBr are enhanced with an increase in temperature, relative to a rapid-iodide addition, (luminescence bands) indicative of different iodide cluster sizes.[1b] The emission spectra are not that of a AgI phase, but of discrete iodide clusters within the defect AgBr lattice; e.g., $(AgI_3)_n$. Control of the hole processes may be monitored by the recombination emission of the $(AgI_3)_n$ center; thus the photographic efficiency may be directed by I^-_m placement, size, and conformation. The shallow electron trap beneath the conduction band may also play a significant role in the photograph process.
5. A 424-nm quantum confinement, 10 K, fluorescence band is observed for all studies in the second-derivative spectra and is attributed to βAgI hexagonal (wurtzite) fine grains of approximately 36 Å diam (Fig. 29). Another photoluminescence band from a prepared, halide excess at –200 mV forms and is large grain, Stokes' shifted to 448 nm and shown in Fig. 11(d). The hexagonal form is not incorporated within the tabular grains. Also, the γAgI sphalerite

cubic form exhibits a microcrystalline emission band at 455 nm.

6. The basic photophysical processes leading to photoluminescence relate to the emulsion-making iodide conditions.
7. The quantum model of a particle-in-a-box provides structural information of bent and linear configuration of iodide cluster centers that reasonably agrees with experimental data. A deviation is observed for the bound single and paired iodide exciton diameter; e.g., 6.6 versus 13.0 Å and 11.0 versus 13.2 Å. The excitons of I_m^{n-} in AgBr may be considered as Wannier excitons characterized by large electron orbitals. The electron–hole separation exceeds the lattice constant of the solid and they are confined separately.
8. Microcrystals containing double-twin planes have an additional excitation band at 461.5 nm (2.6860 eV), the exciton localization at the twin plane. The higher energy excitation is shown at 461.0 nm (2.6889 eV), the assigned indirect exciton band gap. A splitting of 2.9 meV was observed or hole-limiting binding energy to the iodide anion located at the twin plane.
9. From the energy position of the zero-phonon line (2.6402 eV) 469.5 nm, iodide-bound exciton, relative to the indirect exciton gap energy (2.6889 eV) 461.0 nm, the localization energy of the bound state is $E_i = 48.7$ meV with this quantity comprising the binding energy of the hole to the iodide and the electron to the trapped hole minus the free exciton binding energy.
10. The binding energy of 2.9 meV of the exciton relative to the indirect band gap provides an estimate of the hole lifetime (1.41×10^{-10} s) at the double-twin plane at 10 K. The double-twin plane excitation and corresponding emission peak at 461.5 nm (2.860 eV) are thought to be caused by the disturbance of the region crystal symmetry due to the formed interface region; hence, weak trapping of the exciton. The 2.9 meV splitting corresponds to a particle (hole and electron) transit of 188 and 368 Å, respectively, Sample 2, and Sample 1, on excitation within the double-twin plane. Therefore, we may conclude that both hole and electron could traverse the 93.3 and 100 Å plane separations. ◬

Acknowledgments. It gives me great pleasure to thank Dr. S. Chen for the careful TEM characterization of the staking fault dislocation defects and Dr. M. G. Antoniades for the reliable emulsion preparation.

References

1. (a) S. H. Ehrlich, *J. Imaging Sci. Technol.* **39:** 97 (1995); (b) S. H. Ehrlich, *J. Imaging Sci. Technol.* **37:** 73 (1993); (c) S. H. Ehrlich, *J. Imaging Sci. Technol.* **38:** 201 (1994); (d) V. M. Belous, V. P. Cherashov, V. V. Suvorin, F. I. Tolstobron, and Kh. I. Shelekhov, *Shern. Mauch. I. Priklad. Fotogr.i Kinematogr.* **23:** 196 (1978).
2. M. Burberry, *Phys. Rev. B* **37:** 10862 (1989).
3. J. E. Maskasky, *J. Imaging Sci. Technol.* **31:** 15 (1987).
4. W. Czaja, *J. Phys. C.* **16:** 3197 (1983).
5. S. H. Ehrlich, *Photogr. Sci. Eng.* **23:** 348 (1979).
6. P. Junod, H. Hediger, and W. Kundig, *Photogr. Sci. Eng.* **20:** 47 (1976).
7. C. Berry, *J. Photogr. Sci.* **21:** 202 (1973).
8. F. Moser and S. Lyu, *J. Lumin.* **3:** 447 (1971).
9. M. Tsukakashi and H. Kanzaki, *J. Phys. Soc. Jpn.* **30:** 1423 (1970).
10. C. T. Mumaw, *Photogr. Sci. Eng.* **14:** 262 (1970).
11. J. P. Galvan, *Photogr. Sci. Eng.* **14:** 258 (1970).
12. W. Czaja and A. Baldereschi, *J. Phys. C.* **12:** 405 (1969).
13. H. Kanzaki and S. Sakuragi, *J. Phys. Soc. Jpn.* **27:** 109 (1969).
14. F. Moser and F. Urback, *Phys. Rev.* **106:** 852 (1957).
15. G. C. Farnell, P. C. Burton, and R. Hallma, *Philos. Mag.* **41:** 157 (1950); *ibid* 545 (1950).
16. (a) T. M. Mashlyatina, I. V. Nedzvetskaya, N. A. Vidmont, and D. S. Nedzvetski, *Opt. Spectrosc.* **42:** 332 (1977); (b) T. M. Mashlyatina, I. V. Nedzvetskaya, and D. S. Nedzvetski, *Opt. Spectrosc.* (USSR) **46(3):** 343 (1979).
17. T. Barth and G. Lunde, *Zeit. Phys. Chem.* **122:** 293 (1926).
18. M. S. Burberry and Y. T. Tan, Eastman Kodak Company, Research Laboratories, private communication, January 4, 1990.
19. T. Koitabashi and T. Harada, *Soc. Photogr. Sci. Technol. Jpn.* **A4:** 234 (1981), presented May 1981, Annual Meeting, Tokyo, Japan.
20. Y. T. Tan, *J. Photogr. Sci.* **35:** 155 (1987).
21. A. L. Lasker, *Mater. Sci. Forum* **1:** 99 (1984).
22. T. Tani and M. Murofushi, *J. Imaging Sci. Technol.* **38:** 1 (1994).
23. C. Goessens, D. Schryvers, J. Van Landuyt, S. Amelinckx, A. Verbuck, and R. De Keyzer, *J. Cryst. Growth* **110:** 930 (1991).
24. C. Goessens, D. Schryvers, J. Van Landuyt, I. Geuens, R. Gijbels, W. Jacob, and R. De Keyzer, *J. Imaging Sci. Technol.* **39:** 70 (1995).
25. R. W. Berriman and R. H. Henry, *Nature* **180:** 293 (1957).
26. J. F. Hamilton and L. E. Brady, *J. Appl. Phys.* **35:** 415 (1964).
27. (a) J. E. Maskasky, *J. Imaging Sci.* **31(1):** 15 (1987); (b) J. E. Maskasky, *J. Imaging Sci.* **31 (1):** 15 (1987).
28. (a) T. Karasawa, M. Ichida, and T. Komatsu, *Phys. Rev. B* **47:** 1474 (1993); (b) T. Karasawa, T. Komatsu, K. Watanabe, and Y. Kaifu, *J. Phys. Soc. Jpn.* **55:** 897 (1986).
29. (a) W. von der Osten and H. Stolz, *J. Chem. Solids* **51:** 765 (1990); (b) W. von der Osten, H. Stolz, M. Timme, and E. Schreider, *J. Lumin.* **55:** 79 (1993).
30. D. A. Wiegand, *Phys. Rev.* **113:** 59 (1959).
31. G. C. Smith, *Phys. Rev.* **140:** A221 (1965).
32. H. Weller, A Fojtik, and A. Henglein, *Chem. Phys. Lett.* **117:** 485 (1985).
33. J. Wörmer, M. Joppien, G. Zimmer, and T. Möller, *Chem. Phys. Lett.* **172:** 201 (1990).
34. J. I. Steinfeld, J. S. Fransico, W. L. Hase, *Chemical Kinetics and Dynamics,* Prentice Hall Englewood Cliffs, New Jersey, 07632 (1989).
35. L. E. Brus, *J. Phys. Chem.* **90:** 2555 (1986).
36. L. E. Brus, *J. Phys. Chem.* **80:** 4403 (1984); ibid **79:** 5566 (1983).
37. L. E. Brus, *IEEE, J. Quantum Electron* **22:** 1909 (1986).
38. A. Henglein, *Topics Current Chem.* **143:** 113 (1988).
39. A. Henglein, *Chem. Rev.* **89:** 1861 (1989).
40. D. C. Neckers, D. H. Volman, and Gunther von Bünau, Eds., *Advances in Photochemistry,* Vol. **19**, Wiley Interscience, John Wiley & Sons, New York, 1995, p. 179, author Ying Wang.
41. E. W. Washburn, Ed., *International Critical Tables of Numerical Data, Physics, Chemistry and Technology,* McGraw-Hill Book Co., New York, 1930, pp. 7, 21.
42. D. R. Lide, Ed., *CRC Handbook of Chemistry and Physics, 71st ed.,* CRC Press, Boca Raton, Florida, 1990–1991, pp. 12–59.
43. F. Low and D. Pines, *Phys. Rev.* **98:** 414 (1955); J. P. Spoonhower, *J. Phys. Chem. Solids* **51:** 793 (1990).
44. A. Marchetti, *Phys. Rev.* **50:** 12164 (1994).
45. R. Van Heyningen and F. C. Brown, *Phys. Rev.* **111:** 462 (1958).
46. F. C. Brown and K. Kobayashi, *J. Phys. Chem. Solids* **8:** 300 (1959); D. C. Burnam, F. C. Brown, and R. S. Knox, *Phys. Rev.* **119:** 1560 (1961).
47. F. A. Cotton and G. Wilkinson, Eds., *Advanced Inorganic Chemistry,* 5th ed., John Wiley & Sons, New York, 1988, pp. 577-579.